LA-ICPMS, TEM and Raman study of radiation damage, fluid-induced alteration and disturbance of U-Pb and Th-Pb ages in experimentally metasomatised monazite

Bartosz Budzyń [a,*], Richard Wirth [b], Jiří Sláma [c], Łukasz Birski [d], Fabian Tramm [a], Gabriela A. Kozub-Budzyń [e], Grzegorz Rzepa [e], Anja Schreiber [b]

[a] Institute of Geological Sciences, Polish Academy of Sciences (ING PAN), Research Centre in Kraków, Senacka 1, PL–31002 Kraków, Poland
[b] GeoForschungsZentrum Potsdam (GFZ), Section 3.5 Interface Geochemistry, Telegrafenberg, Potsdam 14473, Germany
[c] The Czech Academy of Sciences, Institute of Geology, Rozvojová 269, Prague 6 16500, Czech Republic
[d] Institute of Geological Sciences, Polish Academy of Sciences (ING PAN), Research Centre in Warszawa, Twarda 51/55, PL–00818 Warszawa, Poland
[e] AGH University of Science and Technology, Faculty of Geology, Geophysics and Environmental Protection, al. A. Mickiewicza 30, PL–30059 Kraków, Poland

ARTICLE INFO

ABSTRACT

Experimentally metasomatised monazite was studied in terms of preservation of U-Pb and Th-Pb ages during alkali-bearing fluid-induced alteration over a broad range of temperature conditions 250–750 °C. Starting materials for experiments included Burnet monazite (Concordia age 1100.5 $\pm$ 11.6 Ma, 2σ), albite, K-feldspar, biotite, muscovite, SiO_2, CaF_2, $Na_2Si_2O_5$ and H_2O. Monazite from experiments at 250–550 °C is partially replaced by secondary REE-rich fluorapatite [$(Ca,LREE,Si,Na)_5(PO_4)_3F$], fluorcalciobritholite [$(Ca,REE)_5(SiO_4,PO_4)_3F$] and REE-rich steacyite [$(K,?)(Na,Ca)_2(Th,U)Si_8O_{20}$], and developed patchy zoning, whereas partial replacement by fluorcalciobritholite and cheralite [$CaTh(PO_4)_2$] occurred at 650 and 750 °C, with no signs of compositional alteration based on EPMA data and BSE imaging. Raman microspectroscopy results show narrowing of the $\nu_1(PO_4)$ stretching band in unaltered domains, which indicates advancing annealing of the monazite structure with increasing temperature, and narrow $\nu_1(PO_4)$ band with low FWHM values in altered domains. TEM investigations revealed that unaltered domains of monazite from experiments at 250–550 °C have mottled diffraction contrast, similar to the starting Burnet monazite, which indicates low to moderate degree of metamictization. On the contrary, the altered domains of monazite (patchy zones) show no mottled contrast, suggesting an ordered crystalline structure. TEM imaging demonstrated low degree of metamictization in monazite from the experiment at 650 °C; fluid-aided alteration along the cleavage planes resulted in the development of nanoporosity or partial replacement by fluorcalciobritholite and cheralite. Monazite from the experiment at 750 °C has crystalline structure with no signs of metamictization and shows significant development of nanoporosity and formation of secondary cheralite nanocrystals across the grain. For comparison, TEM and Raman evaluation of xenotime from similar experiments at 350 and 650 °C revealed that both starting xenotime and xenotime from experimental products are crystalline with no signs of radiation damage or fluid-induced alteration affecting internal domains on submicron scale, which could result in compositional alteration of the xenotime.

The unaltered domains of monazite from runs at 250–550 °C yielded U-Pb and Th-Pb dates similar to the age of Burnet monazite, whereas altered domains yielded discordant dates due to various degree of Pb-loss (up to 99.4%). Linear regressions on the Concordia diagrams show lower intercept ages from −266 $\pm$ 160 Ma (run 350 °C, 200 MPa) to −1 $\pm$ 48 Ma (450 °C, 800 MPa), which reflect the "true age" of experimental alteration. The monazite from runs at 650 and 750 °C yielded data indicating initial disturbance of the U-Th-Pb system, ranging from 8.4% Pb-gain to 18.6% Pb-loss. Linear regressions with lower intercepts of −53 $\pm$ 420 Ma and −55 $\pm$ 610 Ma roughly correspond to the timing of the experiments. Furthermore, LA-ICPMS results demonstrate discrepancy between Th-Pb and U-Pb dates suggesting higher mobility of ^{208}Pb than that of ^{207}Pb and ^{206}Pb.

To summarize, TEM and Raman data indicate increasing annealing of the radiation damaged monazite with increasing temperature. Alteration processes induced by alkali-bearing fluid can result in recrystallization of

monazite and various degrees of the age disturbance at temperatures 250–550 °C, whereas isotopic U-Th-Pb microanalysis provide an opportunity to constrain the age of the metasomatic processes as the lower intercept in the Concordia diagram. The particular importance of this study lies in submicron alteration of monazite at 650–750 °C induced by alkali-bearing fluid and/or melt, which remains unnoticed using common electron microscopy BSE imaging. Such alteration, however, induces substantial disturbance of U-Pb and Th-Pb ages, which can cause misinterpretations in reconstructions of geological processes.

1. Introduction

Monazite-(Ce) ((LREE, Th, U)PO$_4$, henceforth monazite) and, to a lesser extent, xenotime-(Y) ((Y, HREE, Th, U)PO$_4$, henceforth xenotime) are common accessory minerals in intermediate and acidic crystalline rocks, and are broadly used in geochronology of igneous, metamorphic and metasomatic processes (Rasmussen, 2005; Williams et al., 2007, 2017; Hetherington et al., 2008; Villa and Williams, 2013; Kylander-Clark, 2017; Schmitt and Vasquez, 2017). Alteration of monazite and xenotime in the presence of alkali-rich fluids and partial replacement by secondary phases were extensively studied in nature (Broska and Siman, 1998; Finger et al., 1998, 2016; Seydoux-Guillaume et al., 2004, 2012; Broska et al., 2005; Hetherington and Harlov, 2008; Janots et al., 2008; Budzyń et al., 2010) and laboratory experiments (Seydoux-Guillaume et al., 2002; Hetherington et al., 2010; Harlov and Hetherington, 2010; Budzyń et al., 2011, 2015, 2017; Harlov et al., 2011; Williams et al., 2011; Budzyń and Kozub-Budzyń, 2015; Grand'Homme et al., 2016, 2018). The compositional alteration via fluid-aided coupled dissolution-reprecipitation processes (cf., Putnis, 2002, 2009) are of particular interest due to their impact on age record. Disturbance of the U-Th-Pb system related to Pb removal by the interacting fluid is relatively common in monazite in granitic and metapelitic rocks (Williams et al., 2017 and references therein), as well as in REE ore deposits (Li et al., 2021). Monazite contains a negligible amount of non-radiogenic Pb (Parrish, 1990), however, recent studies reported the incorporation of considerable amounts of common Pb in monazite from granitic rocks and metapelites (Seydoux-Guillaume et al., 2012; Didier et al., 2013; Holder et al., 2015; Skrzypek et al., 2017; Jastrzębski et al., 2020, 2021; Budzyń et al., 2021), which also has consequences for geochronological applications.

This study presents TEM and Raman revisions of monazite and, to a lesser extent, xenotime from previous experimental works, which were primarily focused on the stability relations of monazite, allanite-(Ce) and apatite, and xenotime, (Y, HREE)-rich epidote and (Y, HREE)-rich apatite in high Ca and Na-Ca environments in a broad P-T range (200–1000 MPa and 250–750 °C; Budzyń et al., 2015, 2017; Budzyń and Kozub-Budzyń, 2015). Electron probe microanalysis (EPMA) measurements in these works revealed partial replacement of monazite by secondary phases and partial removal of Pb in the compositionally altered domains of monazite in experiments at 250–550 °C. At higher temperature conditions of 650 and 750 °C, monazite revealed partial replacement by secondary phases and no compositional alteration. On the contrary, xenotime was more chemically robust during experiments and revealed none or only partial replacement by secondary phases and very limited compositional alteration.

The aim of this study is to evaluate the fluid-induced alteration processes and the degree of radiation damage in monazite from experiments replicating P-T conditions of mid- to upper crustal depths, by using transmission electron microscopy (TEM), electron probe microanalysis (EPMA) and Raman microspectroscopy. Additionally, xenotime from similar experiments was investigated to compare effects of fluid-induced alteration and radiation damage affecting inner parts of the grains with those for monazite. Finally, extensive LA-ICPMS U-Th-Pb investigations of monazite constrained impact of the radiation damage and fluid-induced processes at different experimental conditions from 250 to 750 °C onto preservation (or disturbance) of the U-Pb and Th-Pb ages.

Table 1

Experimental conditions and overview of the experimental products (simplified from Budzyń et al., 2015, 2017; and Budzyń and Kozub-Budzyń, 2015).

Experiment	T (°C)	P (MPa)	Duration (days)	Description
M12N-04	250	200	40	Monazite shows limited porosity and patchy zoning. Small amounts of REE-rich steacyite formed.
M12N-05	350	200	40	Monazite is highly porous and patchy zoned. REE-rich steacyite and REE-rich fluorapatite formed.
M12N-15	350	400	20	Monazite is highly porous and patchy zoned. REE-rich fluorapatite-fluorcalciobritholite and REE-rich steacyite formed.
M12N-10	450	400	18	Monazite is porous along rims or across entire grains, displays patchy zoning and occasionally is partially replaced by REE-rich steacyite. Fluorapatite-fluorcalciobritholite formed.
M12N-23	450	600	16	Monazite is porous along rims or across entire grains, displays patchy zoning and occasionally is partially replaced by REE-rich steacyite. Fluorapatite-fluorcalciobritholite formed.
M12N-16	450	800	16	Monazite is porous along rims or across entire grains, displays patchy zoning and occasionally is partially replaced by REE-rich steacyite. Fluorapatite-fluorcalciobritholite formed.
M12N-02	550	400	6	Monazite is porous along rims or across entire grains and displays patchy zoning. Fluorapatite-fluorcalciobritholite and some REE-rich steacyite formed.
M12N-13	550	800	8	Monazite is porous along rims or across entire grains and displays patchy zoning. Fluorapatite-fluorcalciobritholite formed.
M12N-09	650	200	6	Monazite is strongly dissolved with porosity channels across the grains filled with fluorapatite-fluorcalciobritholite and cheralite. Melt formed.
M12N-08	650	1000	6	Monazite is strongly dissolved with porosity channels across the grains filled with fluorapatite-fluorcalciobritholite and cheralite. Melt formed.
M12N-18	750	200	4	Monazite is partially dissolved with fluorcalciobritholite and cheralite formed on the surface. Melt formed.
X12N-15	350	400	20	Xenotime is partially dissolved on the surface, and occasionally partially replaced by unidentified (Y, HREE)-rich silicate phase.
X12N-09	650	200	6	Xenotime is partially replaced by Y-rich fluorcalciobritholite. Melt formed.
X12N-12	650	600	6	Xenotime is partially replaced by Y-rich fluorcalciobritholite. Melt formed.
X12N-08	650	1000	6	Xenotime is partially replaced by Y-rich fluorcalciobritholite. Melt formed.
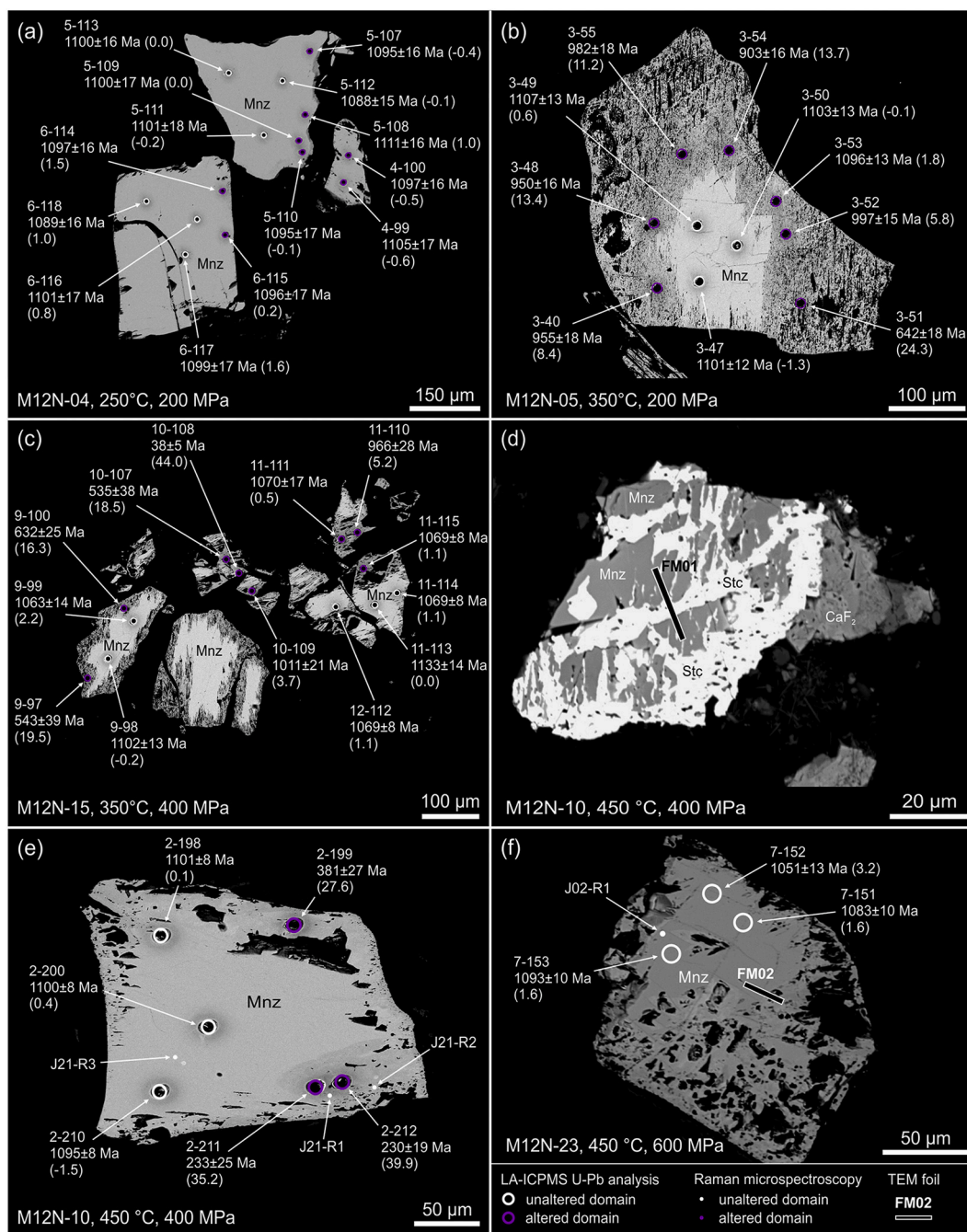
Fig. 1. BSE images of the investigated monazite grains from experiments with marked locations of the FIB-foil lift out, and representative analytical spots of LA-ICPMS U-Pb (discordance values are given in brackets) and Raman microspectroscopy. Analytical labels correspond to data in Table 2 and Supplementary Data Table S3. See text for more explanations. Abbreviations: Brt – fluorcalciobritholite, Cher – cheralite, Mnz – monazite, Stc – REE-rich steacyite.

2. Sample selection and methods

2.1. Sample selection

For this study, monazite and xenotime were selected from the products of experiments conducted under a broad range of P-T conditions ranging from 200 to 1000 MPa and from 250 to 750 °C in earlier experiments (Budzyń et al., 2015, 2017; Budzyń and Kozub-Budzyń, 2015). Representative samples for different P-T conditions were selected (Table 1). Temperature was the primary factor for sample selection, as the previous works have shown that pressure conditions have lesser influence on the alteration of monazite and xenotime.

In all selected experimental products monazite is altered, which includes the development of dissolution pits on the surface, porosity in the altered domains and partial replacement by secondary phases, both overgrowths and inclusions (Fig. 1). Monazite from runs at 250–550 °C shows patchy zoning with irregular boundaries between bright (unaltered) and dark (altered) domains under high contrast EPMA-BSE imaging. The composition of bright domains is similar to the Burnet monazite used as starting material in experiments, whereas the dark domains are compositionally altered, including partial removal of Th, U and Pb (Budzyń et al., 2015, 2017). The secondary phases that replaced monazite include REE-rich fluorapatite [$(Ca,LREE,Si,Na)_5(PO_4)_3F$] and fluorcalciobritholite [$(Ca,REE)_5(SiO_4,PO_4)_3F$] formed during
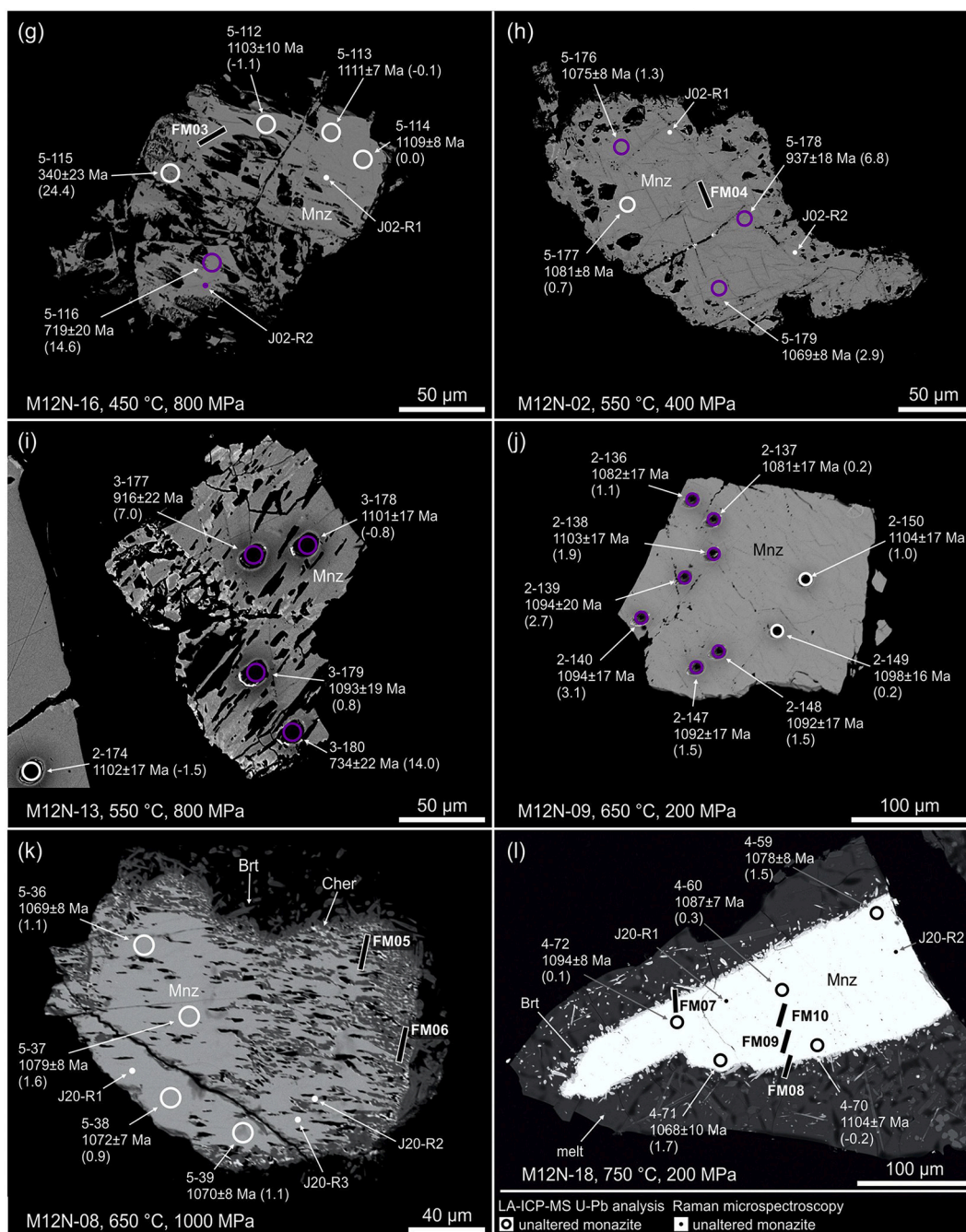
Fig. 1. (*continued*).

experiments at 350–750 °C, REE-rich steacyite [(K,?)(Na,Ca)$_2$(Th,U)Si$_8$O$_{20}$] in experiments at 250–550 °C and cheralite [CaTh(PO$_4$)$_2$] in experiments at 650–750 °C. Experiments at temperature conditions of 650–750 °C resulted in partial melting (Fig. 1l).

A set of altered monazite grains was selected for FIB-foil preparation for TEM studies to investigate alteration on a nanometer-scale in the products of 450–750 °C experiments. The altered monazite from experiments at 250–350 °C was too porous to cut FIB-foils (Fig. 1b, c); however, similar alteration at a less advanced stage is visible in the products of experiments at 450 °C (Fig. 1f, g). Therefore, the monazite material selected for TEM investigations, was representative for all types of alteration. The same samples were selected for Raman microspectroscopy and EPMA measurements to estimate structural disorder in monazite from experiments compared to the fresh Burnet monazite (cf., Ruschel et al., 2012). For the LA-ICPMS U-Th-Pb analysis, representative

samples of monazite were selected from experiments covering temperatures from 250 to 750 °C and different pressures (Table 1, Fig. 1). The isotopic measurements were primarily focused on patchy zoned grains of monazite from runs at 250–550 °C, which were expected to provide data reflecting ca. 0 Ma "age" of the laboratory experiments. Additionally, monazite grains with no features of compositional alteration (homogeneous in BSE imaging) from experiments at 650 °C, 200 and 1000 MPa, and 750 °C, 200 MPa were selected for comparison.

Xenotime from experiments is partially dissolved on the surface with dissolution pits and etching, and partially replaced by secondary (Y, REE)-rich fluorapatite to Y-rich fluorcalciobritholite in all experiments (Fig. 2), except for the low temperature 250–350 °C runs, where an unidentified (Y, HREE)-rich silicate was the main product of xenotime replacement (Fig. 2a). The xenotime grains from all experimental products are homogeneous (i.e. the unreacted cores) with composition
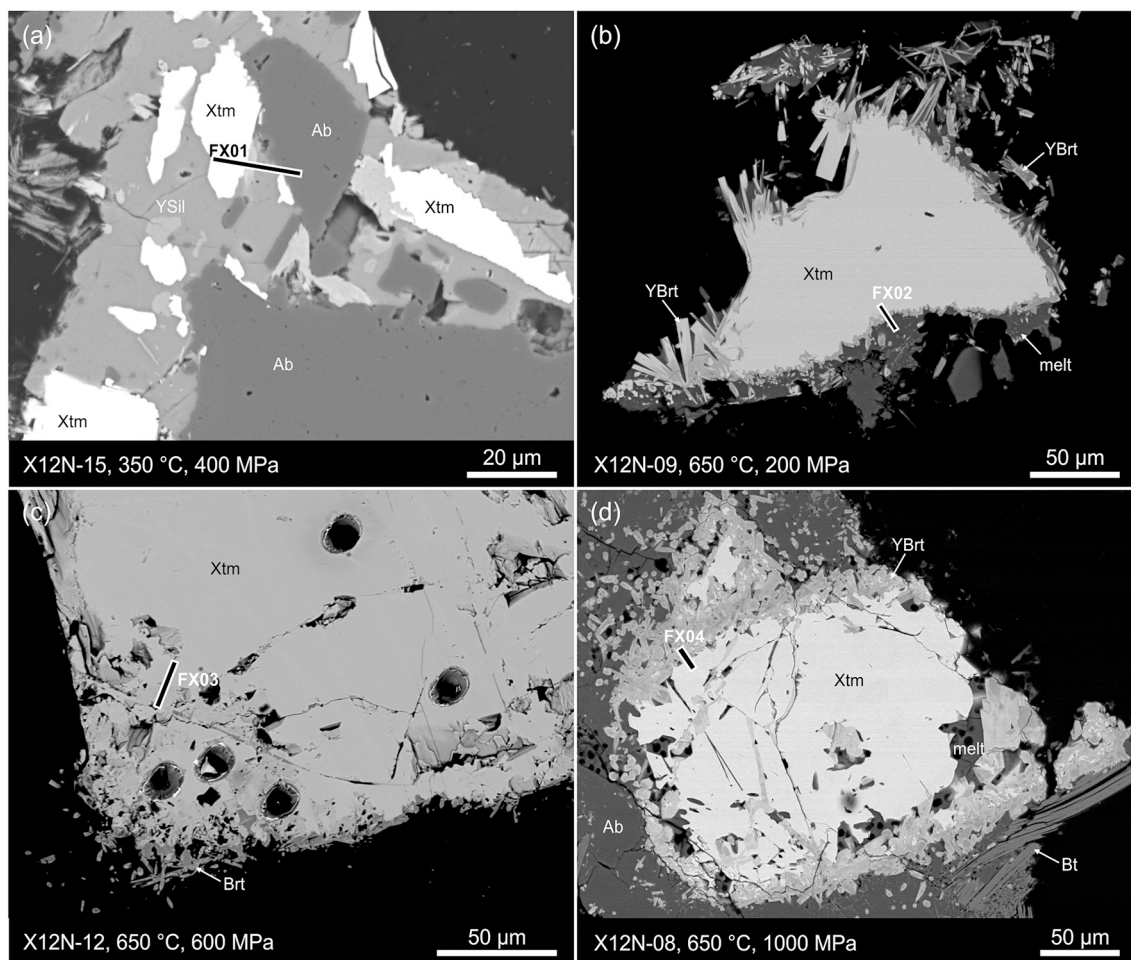
Fig. 2. BSE images of the investigated xenotime grains from experiments with marked locations of the FIB-foil lift out. See text for more explanations. Abbreviations: Ab – albite, Bt – biotite, Xtm – xenotime, YBrt - Y-rich fluorcalciobritholite, YSil – unidentified (Y, HREE)-rich silicate.

similar to that of the starting NWFP xenotime (Budzyń and Kozub-Budzyń, 2015; Budzyń et al., 2017). Recent LA-ICPMS study revealed that xenotime is resistant to alkali-rich fluid, except for limited disturbance of the U-Pb system at 550 and 650 °C due to a fluid-aided coupled dissolution-reprecipitation reactions (Budzyń and Sláma, 2019). Considering that xenotime in experimental products is similar in most of the experimental P-T conditions, one sample representing low-temperature metasomatic alteration (350 °C, 400 MPa) and three samples of xenotime potentially affected by compositional/isotopic alteration (650 °C, 200, 600 and 1000 MPa) were selected for TEM investigations (Fig. 2b–d, Table 1).

To summarize, ten FIB-foils of monazite (FM01–FM10) and four FIB-foils of xenotime (FX01–FX04) from experimental products were investigated with TEM. Additionally, two FIB-foils (FM0 and FX0) from the starting Burnet monazite and NWFP xenotime (Fig. 3) were used as reference materials for evaluation of experimental alteration. Raman microspectroscopy measurements were performed in the same samples (except sample X12N-12) nearby the areas of FIB-foils lift-outs, whenever possible.

2.2. Experimental procedures

Experiments were performed using cold-seal autoclaves on a hydrothermal line (runs at 200 and 400 MPa) and the piston-cylinder apparatus (runs at 600, 800, 1000 MPa) at the Helmholtz Centre Potsdam, GFZ German Research Centre for Geosciences (Potsdam, Germany). Mineral mixes roughly replicated the composition of granitic

rocks. The starting materials included (1) monazite, albite, sanidine, biotite, muscovite, SiO_2, CaF_2, $Na_2Si_2O_5$ and doubly distilled H_2O and (2) xenotime, albite, sanidine, biotite, muscovite, garnet, SiO_2, CaF_2, $Na_2Si_2O_5$ and doubly distilled H_2O. CaF_2 was used as additional source of Ca and F to form fluorapatite, and amorphous SiO_2 was used instead of quartz to increase reaction rates. The Burnet monazite and NWFP xenotime used in experiments originate from a pegmatite from Burnet County (Texas, USA) and a pegmatite from the North-West Frontier Province (NWFP, Pakistan), respectively. The minerals were crushed and sieved to a 50–250 μm fraction. Fine grains were removed by rinsing in ultrasonic bath. Mineral grains with inclusions were hand picked out under the binocular microscope. Starting mixes, including ca. 28.2–36.7 mg of mixed solids and ca. 4.8–5.8 mg of H_2O, were loaded into the 15 mm long and 3 mm wide Au capsules, and arc-welded shut using a Lampert PUK-04 precision welding device. The capsules were checked for leaks by weighing, heating in a 105 °C oven for over 15 h, and then weighing again. After each experiment, the capsules were cleaned, weighed, opened and then dried at 105 °C for over 15 h. A portion of the extracted experimental products was mounted in epoxy and polished for microanalysis. See Budzyń et al. (2017) for more details of experimental procedures.

2.3. Transmission electron microscopy (TEM)

Sample preparation was accomplished by focused ion beam (FIB) milling at the German Research Centre for Geosciences (GFZ Potsdam) using a HELIOS G4 UC FIB/SEM system. Area of 20 × 2 μm on each
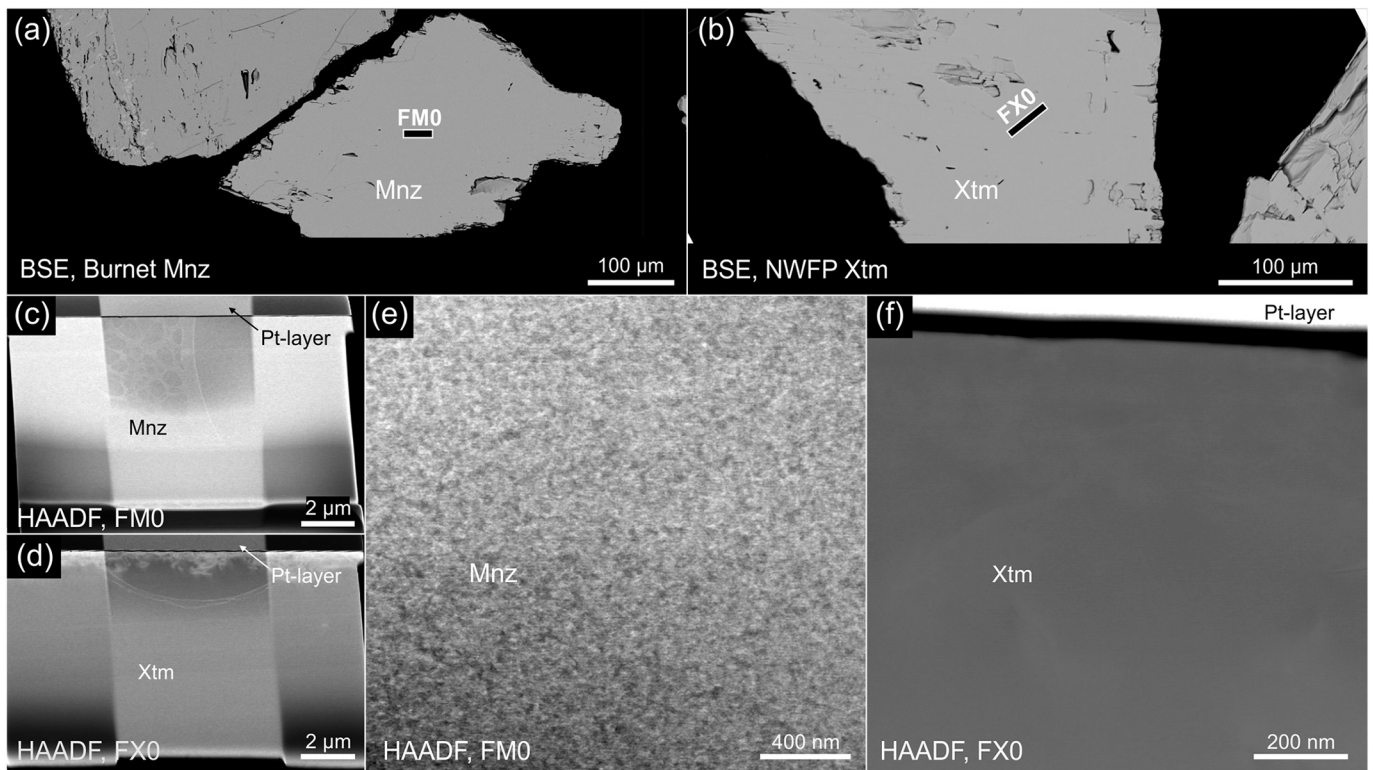
Fig. 3. BSE images (a, b) and TEM-HAADF images (c–f) of the Burnet monazite and NWFP xenotime used as starting materials in experiments. Black lines represent locations of the FIB-foil (c, d) lift out. (e) HAADF image shows a homogeneous, mottled diffraction contrast, which is related to the presence of distorted areas due to moderate irradiation of decaying elements such as Th and U in the monazite (see text for more explanations). (f) HAADF image shows a homogenous and smooth xenotime indicating an intact crystal integrity before the experiments.
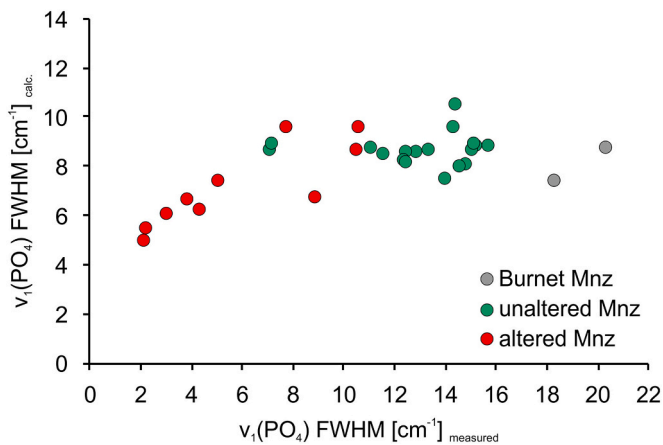
Fig. 4. Diagram presenting the FWHM (full width at half maximum) of measured $\nu_1(PO_4)$ symmetric stretching bands vs. calculated values using EPMA compositional data. The calculated values represent "chemical broadening" of the $\nu_1(PO_4)$ symmetric stretching band (Ruschel et al., 2012). High measured FWHM values in the Burnet monazite indicate moderate degree of metamictization due to radiation damage. Decreasing FWHM values are related to annealing of structural defects in "unaltered" domains due to increasing temperature conditions in experiments or due to recrystallization of "altered" domains due to fluid-mediated coupled dissolution-reprecipitation reactions.

sample was selected. First, a 1.5 μm thick protective layer of Pt was deposited to prevent sample damage caused by FIB sputtering and Ga-ion implantation. Then, material was sputtered out from the frontal and lateral sides of the region of interest, with the FIB operating at an accelerating voltage of 30 kV and a beam current of 47 nA. The rough

cut FIB-sections were lifted out by an Easy-lift system and were fixed on a half-moon shaped Cu grid. The frontal and lateral surface was subsequently thinned with a beam current decreasing from 2.5 nA to 80 pA. The final polishing occurred on both sides with an acceleration voltage of 5 kV and a beam current of 41 pA resulting in a final FIB-foil thickness of approximately 100 nm. The final size of the FIB-foils cut directly from the grains in the thin sections was approximately 20 × 10 × 0.1 μm. No carbon coating was required to prevent charging under the electron beam. See Wirth (2004, 2009) for a detailed description of the sample preparation process.

Transmission electron microscopy observations were performed using a FEI Tecnai G2 F20 X-Twin TEM with a Schottky field emitter as an electron source. The TEM was equipped with a Fishione high-angle annular dark field detector, an EDAX X-Ray analyzer and a Gatan electron energy-loss spectrometer. Different TEM imaging modes such as bright field (BF), high-angle annular dark-field (HAADF), and lattice fringe imaging provided information regarding the transformations of monazite and xenotime in a wide range of P-T conditions. High-resolution lattice fringe images were used to calculate diffraction patterns (fast Fourier transform, FFT). The observed d_{hkl} spacing and the observed angles between adjacent planes were compared with the d_{hkl} spacing and angles calculated from unit cell parameters from literature data. The error in the observed angles must be within $1°$ for positive phase identification. The error in the angular measurements from the FFT was $<0.5°$.

2.4. Raman microspectroscopy

Raman microspectroscopy measurements of monazite and xenotime were performed using a Thermo Scientific DXR Raman Microscope at the Faculty of Geology, Geophysics and Environmental Protection, AGH University of Science and Technology (Kraków, Poland). The Raman

Table 2

Calculated positions and FWHM values (full width at half maximum) of Raman $\nu_1(PO_4)$ stretching band ca. 974 cm^{-1} in monazite and ca. 1000 cm^{-1} in xenotime. See Supplementary Tables S4 and S6 for electronic version.

| Sample	T [°C]	P [MPa]	days	Grain/analysis	Peak position [cm^{-1}]	σ	FWHM[a] [cm^{-1}]	σ	FWHM$_{calc}$[b] [cm^{-1}]	comment
Burnet mnz				J04-R1	973.33	0.022	18.23	0.180	7.46	
				J07-R1	973.60	0.026	20.28	0.056	8.76	
M12N-10	450	400	18	J21-R2	971.27	0.048	2.07	0.214	5.02	Altered (d-r)
				J21-R3	972.46	0.013	13.94	0.188	7.55	Unaltered
				J27-R1p	971.20	0.011	2.15	0.206	5.50	Altered (d-r)
				J27-R2	972.04	0.008	5.00	0.146	7.44	Altered (d-r)
M12N-23	450	600	16	J02-R1	972.03	0.007	2.96	0.082	6.06	Altered (d-r)
				J02-R2	972.09	0.008	3.75	0.184	6.64	Altered (d-r)
				J02-R3	972.33	0.009	4.29	0.192	6.28	Altered (d-r)
				J11-R1	973.71	0.010	8.82	0.180	6.77	Altered (d-r)
				J11-R2	974.90	0.006	15.20	0.022	8.88	Unaltered
M12N-16	450	800	16	J02-R1	972.27	0.010	7.69	0.050	9.65	Altered (d-r)
				J02-R1a	973.13	0.022	15.01	0.088	8.68	Unaltered
				J02-R1b	973.56	0.013	15.66	0.142	8.89	Unaltered
				J02-R2	972.31	0.008	10.47	0.029	8.68	Altered (d-r)
				J02-R2	973.21	0.013	15.09	0.080	8.92	Unaltered
				J10-R1	972.55	0.011	14.78	0.073	8.08	Unaltered
				J10-R2	972.61	0.006	14.53	0.096	8.01	Unaltered
M12N-02	550	400	6	J02-R1	975.35	0.005	14.23	0.098	9.59	Unaltered
				J02-R2	974.93	0.003	14.39	0.013	10.56	Unaltered
				J02-R2–3	973.90	0.041	10.56	0.145	9.64	Altered (d-r)
				J06-R1	973.79	0.004	13.30	0.100	8.66	Unaltered
				J06-R2	974.14	0.008	12.81	0.062	8.57	Unaltered
M12N-08	650	1000	6	J20-R1	973.44	0.009	12.38	0.128	8.60	Unaltered
				J20-R2	973.72	0.007	11.48	0.048	8.55	Unaltered
				J20-R3	973.69	0.005	11.02	0.062	8.81	Unaltered
				J22-R1	972.90	0.007	12.30	0.076	8.25	Unaltered
				J22-R2	973.07	0.008	12.38	0.082	8.18	Unaltered
M12N-18	750	200	4	J20-R1	974.54	0.003	7.07	0.025	8.69	Unaltered
				J20-R2	974.60	0.004	7.16	0.047	8.90	Unaltered
NWFP xenotime				J04-R01	1000.95	0.007	5.53	0.038	4.02	
				J04-R02	1000.56	0.004	5.95	0.007	4.02	
				J06-R01	1000.32	0.004	4.87	0.009	3.96	
				J06-R02	1000.10	0.004	4.85	0.003	3.97	
M12N-15	350	400	20	01a_R01	999.89	0.004	5.25	0.014	4.01	
				01a_R02	999.54	0.004	4.85	0.002	4.03	
				01_R03	1000.07	0.004	4.94	0.005	3.96	
				01_R04	999.70	0.003	4.88	0.005	3.98	
				01_R05	999.85	0.004	4.95	0.002	3.98	
M12N-09	650	200	6	01_R01	1000.16	0.004	4.83	0.005	4.03	
				01_R02	1000.28	0.005	4.87	0.004	4.02	
				01_R03	1000.14	0.006	4.91	0.002	4.03	
M12N-08	650	1000	6	01_R01	1000.00	0.004	4.94	0.007	4.00	
				01_R02	1000.27	0.005	4.83	0.003	3.95	
				01_R03	1000.05	0.005	4.77	0.004	3.95	

[a] FWHM values corrected for instrumental broadening for monazite; measured FWHM values for xenotime.

[b] FWHM values calculated on the basis of Th, U, Ca, and Pb contents using Ruschel et al. (2012) empirical formula for non radiation-damaged monazite: FWHM [cm^{-1}] = 3.95 + 26.66 × (Th + U + Ca + Pb) [a.p.f.u.].

(d-r) stands for dissolution-reprecipitation.
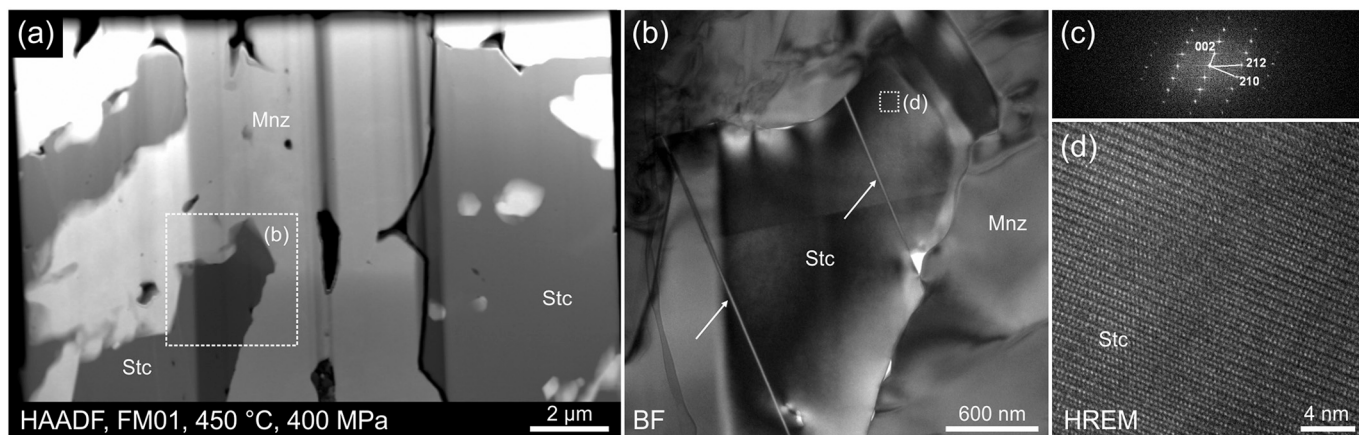
Fig. 5. (a) TEM-HAADF image presenting partial replacement of monazite by REE-rich steacyite in FIB-foil FM01 (experiment M12N-10, 450 °C, 400 MPa, 18 days). (b) BF image of monazite–REE-rich steacyite interface with stacking faults marked with white arrows. (c, d) FFT and HREM lattice fringe image of REE-rich steacyite, presenting structural disorder.
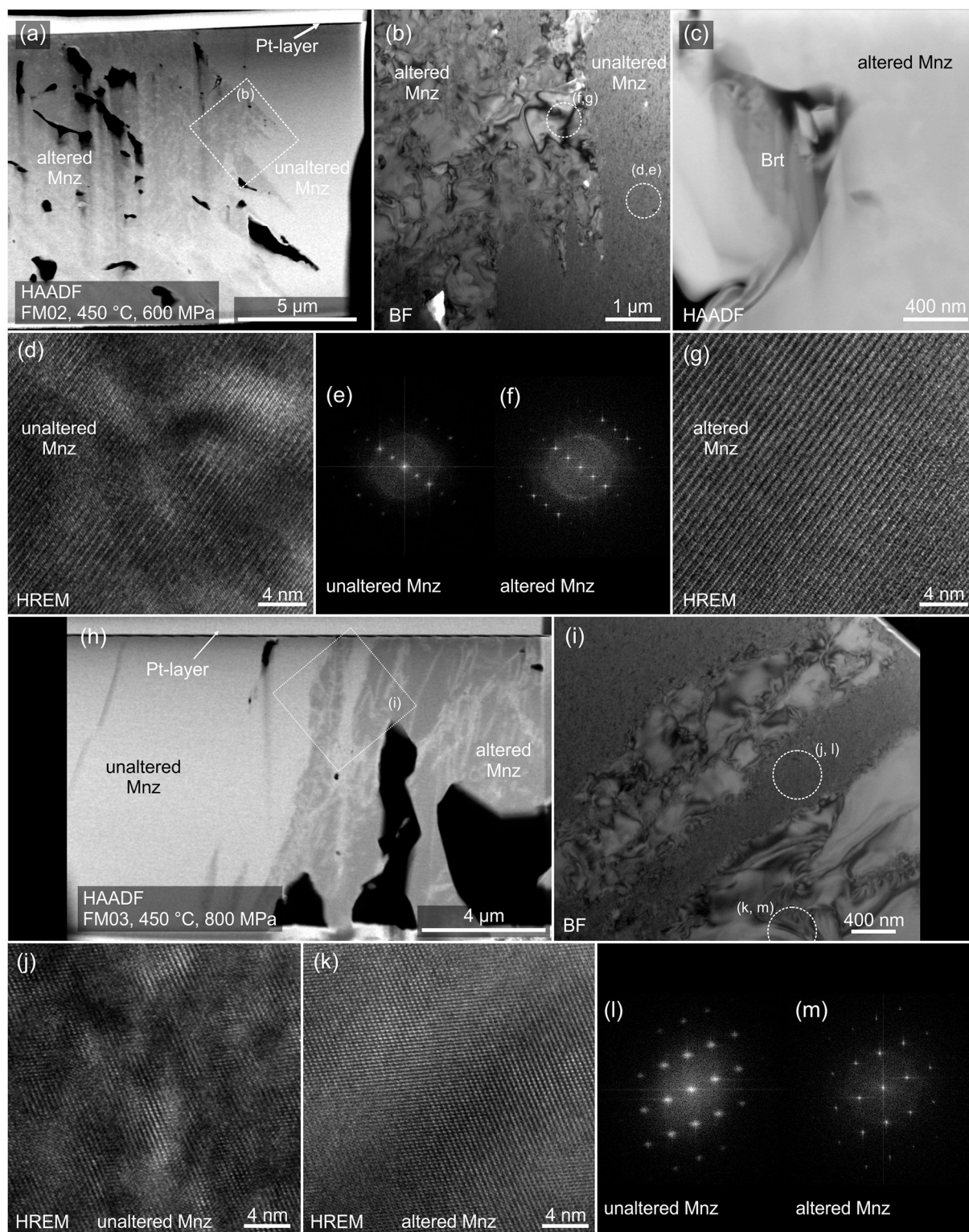
Fig. 6. TEM images demonstrating submicron- to microporosity and microscale patchy zoning developed in monazite from experiments at 450 °C (FIB-foils FM02, experiment M12N-23, 450 °C, 600 MPa, 16 days; and FM03, experiment M12N-16, 450 °C, 800 MPa, 16 days). The unaltered monazite show characteristic mottled diffraction contrast (d, j) and diffuse diffraction spots (e, l) reflecting structural disorder. The altered monazite shows no evidence of structural disorder in HREM and FFT imaging (f, g, k, m). (c) Submicron crystal of secondary fluorcalciobritholite formed in monazite in experiment at 450 °C, 600 MPa, 16 days.

spectra were recorded at room temperature using a 900 grooves/mm grating, a CCD detector, an Olympus 100× objective and a spot size of ca. 0.7 μm). A 532 nm diode laser with a power of 10 mW, an exposure time of 3 s and 100 data accumulations were used. The Raman spectra were fitted after background correction assuming Gaussian-Lorentzian band shape (Ruschel et al., 2012). The measured FWHMs (full width at half maximum) values of the most intense $\nu_1(PO_4)$ stretching band at ca. 971–975 cm^{-1} in monazite were corrected for instrumental

broadening of the Raman spectrometer (Nasdala et al., 2001).

### 2.5. Electron probe microanalysis (EPMA)

Compositional analyses of monazite and xenotime were performed after Raman measurements, and in the same spots, by using a JEOL SuperProbe JXA-8230 electron microprobe equipped with five wavelength dispersive spectrometers at the Laboratory of Critical Elements AGH–KGHM at the AGH University of Science and Technology (Kraków, Poland). Analytical conditions included an accelerating voltage of 15 kV, a probe current of 100 nA and a beam size of 3 μm (see Supplementary Table S1 for further analytical details). Data were corrected to the ZAF procedure using in-house JEOL software.

2.6. Laser ablation inductively coupled plasma mass spectrometry (LA-ICPMS)

A Thermo Scientific Element 2 sector field ICP-MS coupled to a 193 nm ArF excimer laser (Teledyne Cetac Analyte Excite laser) at the Institute of Geology of the Czech Academy of Sciences, Prague, Czech Republic, was used to measure the Pb/U, Pb/Th and Pb isotopic ratios in monazite and xenotime. The analytical details are provided as supplementary material. No common Pb correction was applied to the data due to the high Hg contamination of the commercially available He carrier gas, which precludes accurate correction of the interfering ^{204}Hg on the very small signal of ^{204}Pb (common lead). The U-Pb dates are presented as Concordia plot generated with ISOPLOT v. 4.16 (Ludwig, 2012).
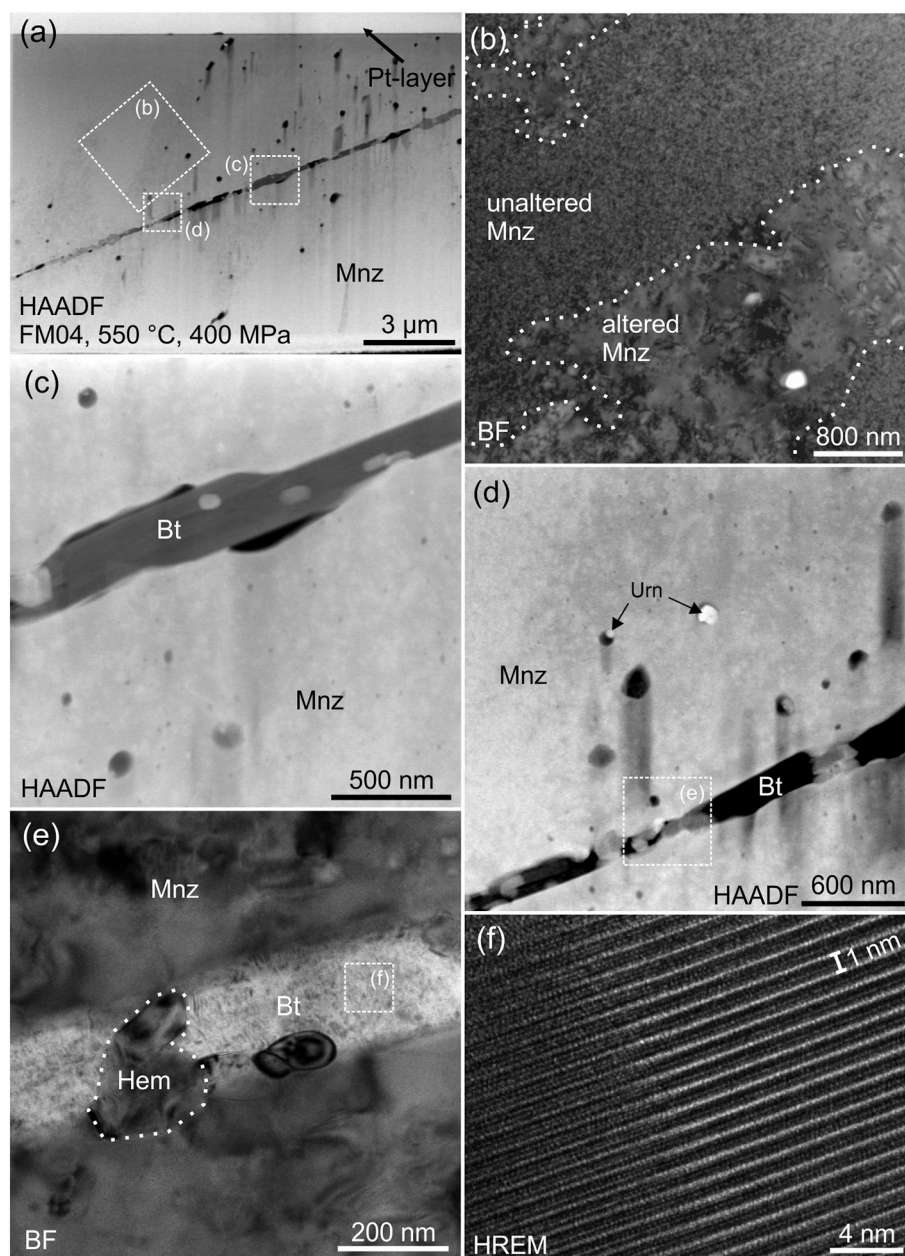
Fig. 7. TEM images showing monazite altered along and close to cleavage planes (FIB-foil FM04, 550 °C and 400 MPa). The altered monazite domains demonstrate a mottled diffraction contrast related to structural disorder (b, d). The cracks in monazite are filled with biotite (Bt) and hematite (Hem) (c–e), whereas uraninite (Urn) occasionally formed in the nanopores (d). (f) The biotite lattice fringe image displays a distance of the basal planes of 1 nm.
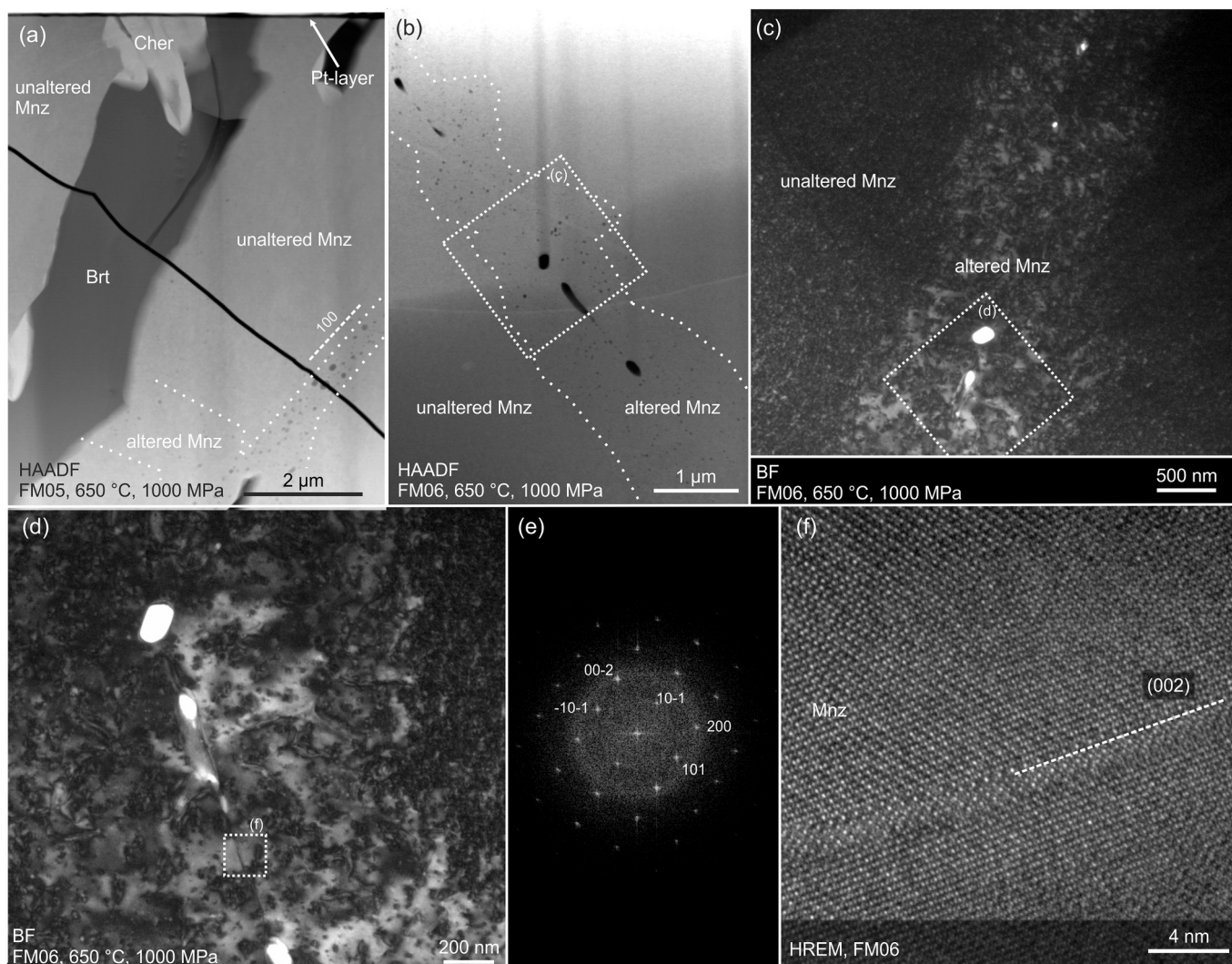
Fig. 8. TEM images of the monazite from experiment at 650 °C and 1000 MPa (FIB-foils FM05 and FM06). Altered monazite domains contain nanoporosity occasionally showing clear patterns of elongated pores along cleavage. Stronger alteration resulted in partial replacement by fluorcalciobritholite and cheralite. The altered monazite demonstrates high degree of crystallinity nearby nanopores oriented along cleavage axis (002), which represent fluid-penetration pathways.

3. Results

### 3.1. TEM and Raman microspectroscopy – monazite

The Burnet monazite demonstrates a homogeneous, mottled diffraction contrast in HAADF mode (Fig. 3e), which is related to slightly distorted crystal subunits of nanometer size. A moderate degree of structural radiation damage is also reflected in broadening of $\nu_1(PO_4)$ band showing 18.23–20.28 cm^{-1} FWHM values, which are significantly higher than calculated FWHM values of 7.46–8.76 cm^{-1} corresponding to the composition of non-radiated monazite (Fig. 4, Table 2).

Monazite in FIB-foil FM01 (450 °C, 400 MPa, 18 days) displays a sharp and distinct interface with secondary REE-rich steacyite (Fig. 5a, b). Porosity is present within monazite and at the interface between monazite and REE-rich steacyite (Fig. 5a, b). The REE-rich steacyite contains planar defects expressed as stacking faults (Fig. 5b). Raman data of monazite demonstrate significant discrepancy between measured FWHM values of $\nu_1(PO_4)$ band, which are 13.94 cm^{-1} and 2.07–5.00 cm^{-1} in unaltered and altered domains of monazite, respectively (Fig. 4, Table 2).

Two FIB-foils with monazite from two other experiments at 450 °C (FM02, run at 600 MPa, 16 day; FM03, run at 800 MPa, 16 days) show cross sections between unaltered and altered, patchy domains (Fig. 1f,

g), which are bright and dark, respectively, in HAADF imaging (Fig. 6a, h). Microporosity with minor submicron pores developed in the altered domains. The unaltered domains are homogeneous and show patchy or mottled diffraction contrast in BF imaging (Fig. 6b, i), mottled diffraction contrast in HREM imaging (Fig. 6d, j) and diffuse diffraction intensity (Fig. 6e, l). The diffuse diffraction intensity is due to a slight misorientation of the scattering subunits in the crystal, which also cause the mottled diffraction contrast. The altered domains are homogenous and crystalline in BF imaging, with no cracks, dislocations or low-angle grain boundaries (Fig. 6b, i). They also show high crystallinity in HREM imaging (Fig. 6g, k), and undisturbed and sharp diffraction patterns (Fig. 6f, m). The interface between both domains is mostly irregular, although altered domains partially proceeded along specific direction related to crystallographic orientation (Fig. 6a, b). The measured FWHM values for $\nu_1(PO_4)$ stretching band in unaltered and altered domains are 14.53–15.66 cm^{-1} and 2.96–10.47 cm^{-1} respectively (Fig. 4, Table 2).

The monazite in FIB-foil FM04 from experiment at 550 °C, 400 MPa and 6 days shows patchy zoning (Fig. 1h), but less intensely developed compared to monazite from runs at 450 °C. The bright domain in HAADF imaging shows a mottled contrast in BF imaging (Fig. 7a, b), similarly to the Burnet monazite. The altered domain (dark in HAADF imaging) is crystalline with remnants of patches with mottled contrast in BF imaging, and contains minor inclusions of uraninite and nanopores
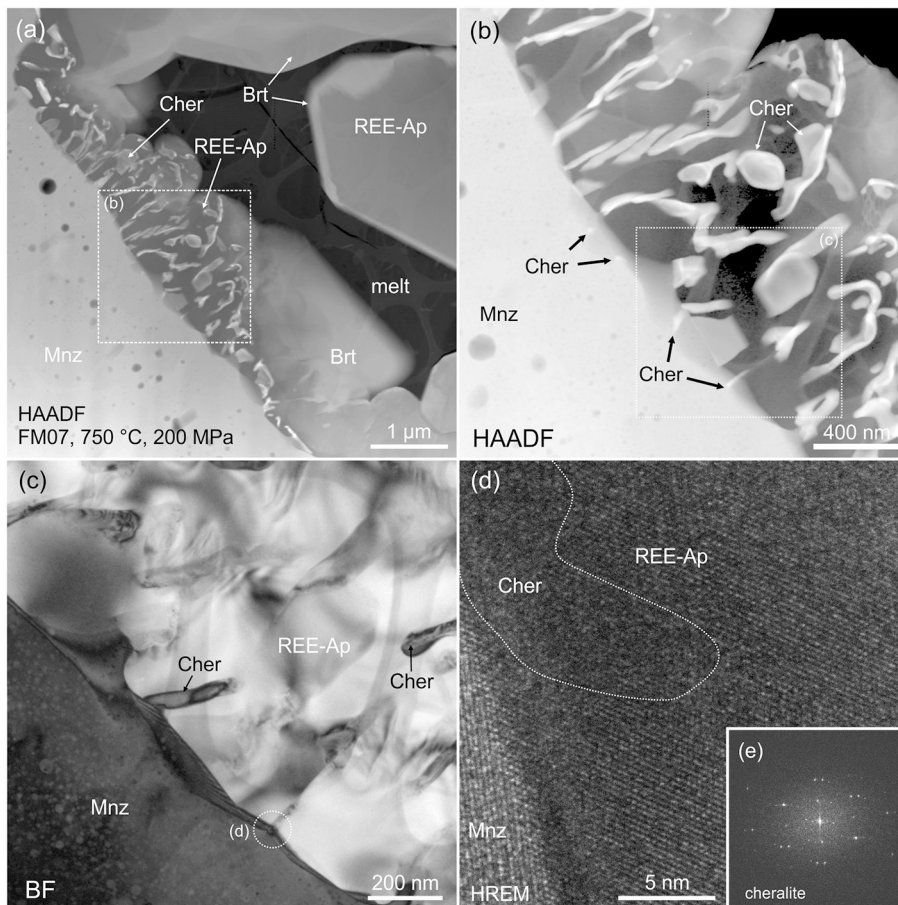
Fig. 9. TEM images of four FIB-foils lift-out from single monazite grain from experiment at 750 °C and 200 MPa (FIB-foils FM07–FM10). Experimental metasomatism resulted in partial replacement of monazite by fluorcalciobritholite, REE-enriched fluorapatite and cheralite, which form flame-like textures at the monazite grain surface. Nucleation centers of cheralite directly at the surface of monazite are marked with black arrows at (b). The reaction front is presented as the phase boundary between monazite and REE-enriched fluorapatite (d) with nucleating cheralite (e). Nanoporosity developed across the monazite grain, both in the rim and the core, with occasional nanoinclusions of secondary cheralite (h, l). See text for more explanations.

(Fig. 7a, b, d). Cracks in monazite are filled with submicron grains of biotite and hematite (Fig. 7c–f). The measured FWHM values for $\nu_1(PO_4)$ stretching band are 12.81–14.39 cm^{-1} and 10.56 cm^{-1} in unaltered and altered domains, respectively (Fig. 4, Table 2).

The monazite from experiment at 650 °C and 1000 MPa (FIB-foils FM05 and FM06; Fig. 1k) is partially replaced by fluorcalciobritholite and cheralite. Monazite reveals faint altered domains (Fig. 8), which are too small for identification using EPMA-BSE imaging. The unaltered domains show no porosity on submicron scale, and display mottled diffraction contrast in BF imaging due to irradiation damage (Fig. 8c). The altered domains are oriented along the cleavage of (001,100) (Fig. 8a, b, f) and reveal high crystallinity due to healing of the irradiation damage with only patches of mottled contrast in BF imaging (Fig. 8c–f). Nanopores present in the altered domain demonstrate patterns of connection along the cleavage (Fig. 8c, d, f). The measured FWHM values for $\nu_1(PO_4)$ Raman band in unaltered monazite are 11.02–12.38 cm^{-1} (Fig. 4, Table 2).

Monazite from experiments at 750 °C, 200 MPa and 6 days is overgrown by REE-rich fluorapatite and fluorcalciobritholite with submicron inclusions of cheralite that form flame-like microtexture (Fig. 1l, 9). Cheralite precipitation centers occur at the surface of monazite and the transition to REE-rich fluorapatite. The diffraction patterns of cheralite suggest the presence of polycrystals with different crystallographic orientations (Fig. 9e). The monazite crystals in two FIB-foils lifted out from the core of the crystal (FM09 and FM10, Fig. 1l) show crystalline structure with numerous nanopores in HAADF imaging (Fig. 9h, l), and a good crystallinity in HREM imaging and diffraction patterns (Fig. 9j, k). Monazite also contains minor nanoinclusions of cheralite nucleated in nanopores. The measured FWHM values for $\nu_1(PO_4)$ Raman band in monazite are 7.07–7.16 cm^{-1}, which are closest to calculated values of

8.69–8.90 cm^{-1} corresponding to the composition of non-radiated monazite (Fig. 4, Table 2).

3.2. LA-ICPMS U-Th-Pb analysis – monazite

LA-ICPMS U-Th-Pb analyses were performed in 4–12 monazite grains, depending on the availability in the experimental products from each run. 28 analyses in 11 grains of the Burnet monazite (used as a starting material) yielded $^{207}Pb/^{235}U$ dates from 1090 ± 16 to 1116 ± 16 Ma (2σ, disc. from −0.9 to +1.5%), $^{208}Pb/^{232}Th$ dates from 1065 ± 14 to 1109 ± 15 Ma (2σ, Table 3) and a Concordia age of 1100.5 ± 11.6 Ma (2σ, MSWD = 0.12; Fig. 10a). The individual analyses revealed similar values of "Pb-loss" (up to 1.6%) or "Pb-gain" (up to 2.6%; Fig. 11a) calculated with respect to average isotopic $^{207}Pb/^{235}U$ and $^{208}Pb/^{232}Th$ ratios in the Burnet monazite (Table 3). Such values are in line with expected variation between individual analyses of a single population and within the current limits of LA-ICPMS geochronology, which is at best 2–4% for individual analysis and 1% for weighted mean (Schaltegger et al., 2014; Schoene, 2014; Horstwood et al., 2016). Henceforth, the values calculated from the isotopic data yielded by monazite from experimental products, which stay outside of range ± 2.5% are interpreted as indicative for fluid-mediated removal (or gain) of Pb. Summary of the U-Th-Pb data is presented in Table 3 and Fig. 10, whereas complete U-Th-Pb dataset is presented in Supplementary Data Table S3.

All experiments resulted in a varying degree of isotopic disturbance in the monazite. Minor to major development of compositionally altered domains (including patchy zoning, low- to high porosity and inclusions of secondary phases), which affected rims to entire grains formed in runs under temperature conditions from 250 to 550 °C. $^{207}Pb/^{235}U$ and
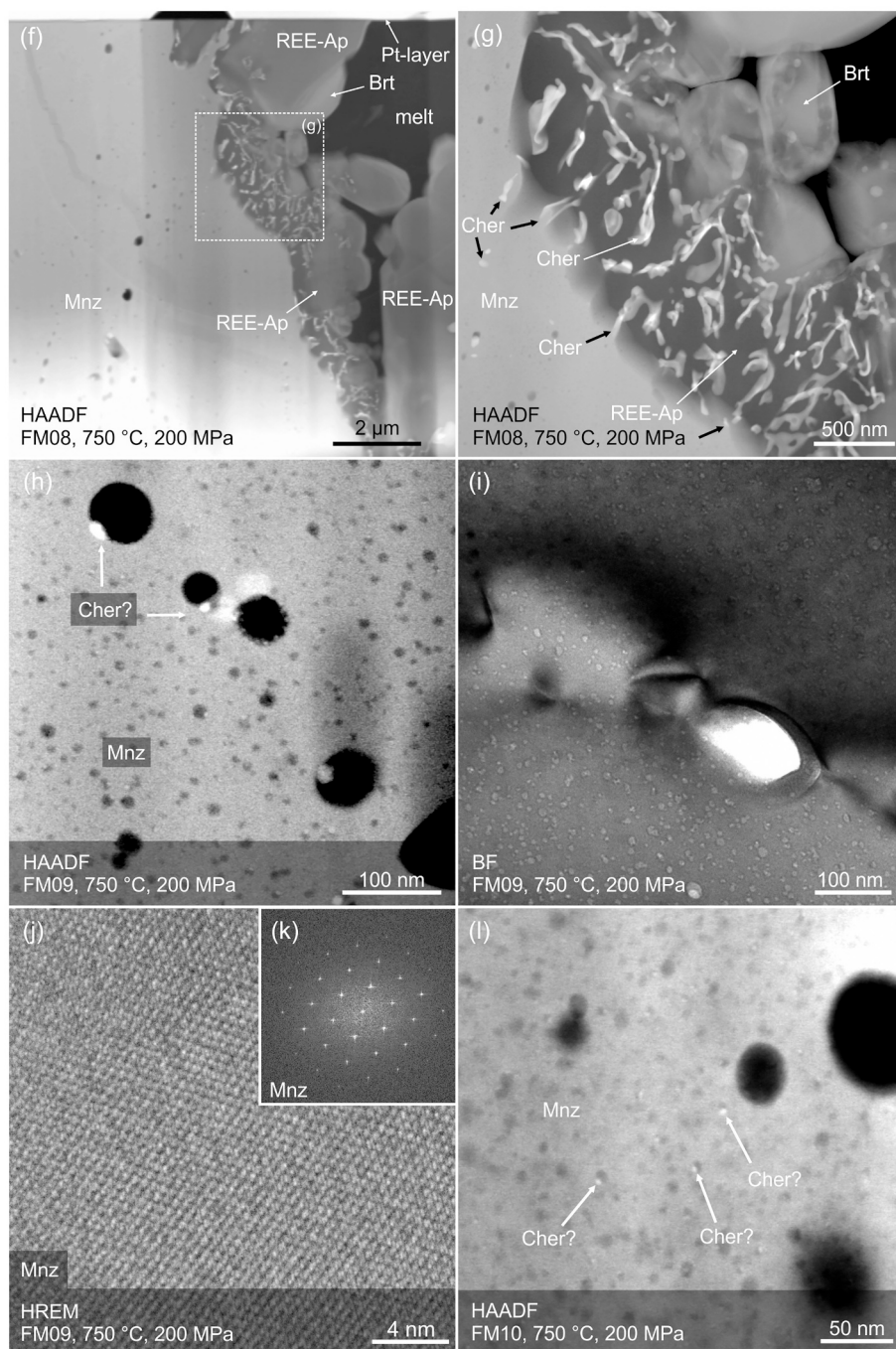
^{208}Pb/^{232}Th dates in unaltered domains are mostly within error to those of the fresh Burnet monazite, with some exceptions suggesting gain or removal of Pb (Table 3, Fig. 11b–i). U-Th-Pb data from the altered domains show significant discrepancies between ^{207}Pb/^{235}U and ^{208}Pb/^{232}Th dates, which range from (i) 38 ± 5 vs. 18 ± 1 Ma (M12N-15, 350 °C, 400 MPa), 230 ± 19 vs. 15 ± 2 Ma (M12N-10, 450 °C, 400 MPa) or 59 ± 10 vs. 7 ± 0 Ma (M12N-23, 450 °C, 600 MPa) to (ii) 1174 ± 10 vs. 1117 ± 15 Ma (M12N-10, 450 °C, 400 MPa). The fluid-aided Pb-loss during experimental alteration affected monazite most significantly in experiments under conditions of 250–450 °C. The discrepancies between calculated Pb-loss values are consistently lower for ^{207}Pb/^{235}U isotope ratios compared to those for ^{208}Pb/^{232}Th isotope ratios, reaching up to 98.0% vs. 98.4% "Pb-loss" (M12N-15, 350 °C, 400 MPa), 86.6% vs. 98.6% (M12N-10, 450 °C, 400 MPa), and 96.7% vs. 99.4% (M12N-23,

450 °C, 600 MPa) in altered monazite domains (Fig. 11, Table 3). The discordant U-Pb data in runs at 250–550 °C show upper intercept dates from 1097.2 ± 6.0 Ma to 1119 ± 19 Ma, which are within error of 1100.5 ± 11.6 Ma Concordia age of the Burnet monazite (Fig. 10a–i). The lower intercept dates range from −266 ± 160 Ma to −1 ± 48 Ma, mostly staying within error of 0 Ma, i.e. "age" of the experiment (Fig. 10b–i). The higher uncertainties of the lower intercept values are given by lower Pb counts in samples with significant Pb-loss.

The monazite from experiments at 650 °C reveal faint patchy zoning considered a result of experimental alteration. The unaltered domains yielded ^{207}Pb/^{235}U and ^{208}Pb/^{232}Th dates with slightly broader range compared to those of the original Burnet monazite, i.e. from 1054 ± 8 to 1113 ± 17 Ma and from 1033 ± 14 to 1094 ± 17 Ma, respectively (Table 3). The altered domains yielded ^{207}Pb/^{235}U dates from 945 ± 21

Table 3

Summary of $^{207}Pb/^{235}U$ and $^{208}Pb/^{232}Th$ monazite data for the Burnet monazite (starting material) and monazite from the experimental products with calculated values of fluid-induced Pb-loss (negative values reflect Pb-gain). Altered domains are distinguished based on the textural features of experimentally altered monazite, i. e. the presence of porous or patchy domains. Complete U-Th-Pb dataset is presented in Supplementary Data Table S3.

Sample	Comment	n	$^{207}Pb/^{235}U$ date (Ma) (2σ)		$^{208}Pb/^{232}Th$ date (Ma) (2σ)		Disc. (%)[a]		Pb-loss$^{207/235}$ (%)[b]		Pb-loss$^{208/232}$ (%)[c]	
			min	max	min	max	min	max	min	max	min	max
Burnet monazite	Starting material	28	1090 ± 16	1116 ± 16	1065 ± 14	1109 ± 15	−0.9	1.5	−2.6	1.5	−2.5	1.6
M12N-04	unalt. dom.	32	1082 ± 16	1141 ± 14	1053 ± 14	1209 ± 16	−1.1	1.6	−6.5	2.6	−12.1	2.7
250 °C, 200 MPa, 40 days	alt. dom.	16	259 ± 13	1137 ± 17	145 ± 5	1184 ± 17	−1.9	36.8	−5.9	84.9	−9.8	86.8
M12N-05	unalt. dom.	6	1079 ± 13	1107 ± 13	974 ± 13	1138 ± 13	−1.3	0.8	−1.2	3.0	−5.4	10.4
350 °C, 200 MPa, 40 days	alt. dom.	15	642 ± 18	1115 ± 16	113 ± 2	891 ± 23	0.2	24.2	−2.8	54.4	18.0	89.8
M12N-15	unalt. dom.	20	1063 ± 14	1154 ± 16	982 ± 20	1124 ± 18	−1.7	2.4	−8.3	5.2	−4.0	9.5
350 °C, 400 MPa, 20 days	alt. dom.	22	38 ± 5	1140 ± 16	18 ± 1	1106 ± 17	−2.8	44.0	−6.5	98.0	−2.3	98.4
M12N-10	unalt. dom.	16	754 ± 40	1129 ± 10	560 ± 48	1156 ± 17	−1.5	9.7	−4.6	38.2	−7.0	48.5
450 °C, 400 MPa, 18 days	alt. dom.	12	230 ± 19	1174 ± 10	15 ± 2	1117 ± 15	−0.6	39.9	−11.6	86.6	−3.3	98.6
M12N-23	unalt. dom.	14	1051 ± 13	1114 ± 18	1104 ± 21	1115 ± 16	−1.4	3.2	−2.4	6.9	−3.1	7.4
450 °C, 600 MPa, 16 days	alt. dom.	28	59 ± 10	877 ± 29	7 ± 0	574 ± 23	8.4	43.1	27.7	96.7	47.5	99.4
M12N-16	unalt. dom.	25	1083 ± 10	1146 ± 12	1032 ± 20	1174 ± 18	−2.4	1.0	−7.4	2.3	−8.7	4.7
450 °C, 800 MPa, 16 days	alt. dom.	14	340 ± 23	1156 ± 13	130 ± 5	1161 ± 16	−3.6	24.4	−8.9	78.6	−7.4	88.3
M12N-02	unalt. dom.	16	1011 ± 10	1122 ± 9	943 ± 23	1108 ± 15	−0.6	4.5	−3.3	12.7	−2.5	13.1
550 °C, 400 MPa, 6 days	alt. dom.	3	937 ± 18	1075 ± 8	1059 ± 14	1083 ± 13	1.3	6.8	3.7	21.3	−0.1	2.2
M12N-13	unalt. dom.	13	1094 ± 17	1107 ± 17	1063 ± 15	1109 ± 21	−1.5	0.7	−1.0	0.7	−2.6	1.8
550 °C, 800 MPa, 8 days	alt. dom.	4	734 ± 22	1101 ± 17	456 ± 21	1088 ± 16	−0.8	14.0	−0.4	44.8	−0.6	58.5
M12N-09	unalt. dom.	10	1090 ± 16	1113 ± 17	1056 ± 14	1094 ± 17	−0.5	1.7	−1.9	1.3	−1.1	2.4
650 °C, 200 MPa, 6 days	alt. dom.	14	1065 ± 17	1105 ± 20	1044 ± 16	1085 ± 18	0.1	3.1	−0.8	4.8	−0.3	3.6
M12N-08	unalt. dom.	23	1054 ± 8	1100 ± 9	1033 ± 14	1078 ± 13	−0.4	3.1	0.2	6.6	0.4	4.6
650 °C, 1000 MPa, 6 days	alt. dom.	1	956 ± 21	–	927 ± 25	–	5.4	–	18.6	–	14.7	–
M12N-18	unalt. dom.	15	1068 ± 10	1130 ± 9	1057 ± 18	1170 ± 16	−1.5	2.7	−4.5	4.8	−8.4	2.3
750 °C, 200 MPa, 4 days	alt. dom.	–	–	–	–	–	–	–	–	–	–	–

Notes: unalt. dom. – unaltered domain; alt. dom. – altered domain.

  [a] disc. = $(1 - {}^{206}Pb/{}^{238}U/{}^{207}Pb/{}^{235}U) \times 100$.

  [b] Pb-loss $({}^{207}Pb/{}^{235}U) = ({}^{207}Pb/{}^{235}U_{BrtMnz\ Ave} - {}^{207}Pb/{}^{235}U_{measured}) \times 100/{}^{207}Pb/{}^{235}U_{BrtMnz\ Ave}$.

  [c] Pb-loss $({}^{208}Pb/{}^{232}Th) = ({}^{208}Pb/{}^{232}Th_{BrtMnz\ Ave} - {}^{208}Pb/{}^{232}Th_{measured}) \times 100/{}^{208}Pb/{}^{232}Th_{BrtMnz\ Ave}$.

Ma to 1105 ± 20 Ma and $^{208}Pb/^{232}Th$ dates from 927 ± 25 to 1085 ± 18 Ma. The calculated fluid-aided Pb-loss reached 18.6 and 14.7%, but also up to 4.8 and 3.6% Pb-gain for $^{207}Pb/^{235}U$ and $^{208}Pb/^{232}Th$ ratios, respectively, in altered domains. However, the unaltered domains also show up to 6.6 and 4.6% Pb-loss for $^{207}Pb/^{235}U$ and $^{208}Pb/^{232}Th$ ratios, respectively. The U-Pb data are slightly discordant and provided an upper intercept date of 1111 ± 13 Ma and a lower intercept date of −762 ± 1400 Ma in run at 650 °C and 200 MPa; and an upper intercept date of 1106 ± 19 Ma and a lower intercept date of −53 ± 420 Ma in run at 650 °C and 1000 MPa (Fig. 10j, k),

The monazite grains from experiment at 750 °C and 200 MPa are homogeneous in BSE imaging with no signs of alteration affecting internal parts of the grains. The monazite yielded $^{207}Pb/^{235}U$ dates from 1068 ± 10 to 1130 ± 9 Ma and $^{208}Pb/^{232}Th$ dates from 1057 ± 18 to 1170 ± 16 Ma (Table 3). These reflect ca. 4.8% Pb-loss to 4.5% Pb-gain for $^{207}Pb/^{235}U$ ratio and ca. 2.3% Pb-loss to 8.4% Pb-gain for $^{208}Pb/^{232}Th$ ratio. The discordant U-Pb data provided an upper intercept date of 1111 ± 15 Ma and a lower intercept date of −55 ± 610 Ma (Fig. 10l).

3.3. TEM and Raman microspectroscopy – xenotime

The NWFP xenotime is homogeneous in HAADF imaging and shows no evidence of structural disorder related to radiation damage (Fig. 3f). The measured FWHM values for $\nu_1(PO_4)$ Raman band ca. 1000 cm^{-1} are 4.85–5.95 cm^{-1}, which are slightly higher than 3.96–4.02 cm^{-1} values (Table 2) representing FWHM values of the non-radiated structure.

FIB-foil FX01 lifted out from the xenotime and secondary phases from experiment at 350 °C, 400 MPa and 20 days (Fig. 2a), shows a sharp boundary between xenotime, Y-rich fluorcalciobritholite and unidentified (Y, HREE)-rich silicate (Fig. 12). The nanocrystals of unidentified (Y, HREE)-rich silicate, located between the xenotime surface and Y-rich fluorcalciobritholite, show differences in diffraction contrast in BF imaging, as well as mottled diffraction contrast in HREM imaging

and smeared out diffraction patterns, which indicate differences in their crystallographic orientation (Fig. 12b, c, e). The amorphous layer formed between the xenotime and Y-rich fluorcalciobritholite contains nanocrystals of Y-rich fluorcalciobritholite observed in HREM imaging (Fig. 12e). The measured FWHM values for $\nu_1(PO_4)$ Raman band are 4.85–5.25 cm^{-1}, staying close to the FWHM values of the fresh NWFP xenotime (Table 2).

Three FIB-foils with the xenotime from experiments at 650 °C were investigated: FM02 (run at 200 MPa, 6 days), FM03 (600 MPa, 6 days) and FM04 (1000 MPa, 6 days) (Fig. 2b–d). The xenotime shows mostly sharp and distinct phase boundaries with secondary Y-rich fluorcalciobritholite crystals in HAADF and BF imaging (Fig. 13a, b, e–g). Submicron scale pores occur only occasionally between these phases (Fig. 13e). HREM imaging and diffraction patters indicate high crystallinity of xenotime from runs at 650 °C, with no distinct defects or alteration (Fig. 13c, h), similarly to the NWFP xenotime. The measured FWHM values for $\nu_1(PO_4)$ Raman band are 4.83–4.91 cm^{-1} and 4.77–4.94 cm^{-1} (in experiments at 650 °C, 200 MPa and 650 °C, 1000 MPa, respectively), which are similar to those of the NWFP xenotime (Table 2).

4. Discussion

The main interest of our study is focused on the processes that may affect the U-Th-Pb age record, which are driven by coupled dissolution-reprecipitation reactions induced by alkali-bearing fluids (e.g., Williams et al., 2011). The altered, patchy domains are usually considered as those that provide the true age of metasomatic processes. Therefore, the crucial question is, whether we can identify such alteration by using common microanalytical techniques, such as EPMA-BSE imaging or compositional X-ray mapping. Uncompleted re-equilibration, partial Pb-loss or other disturbance of the U-Th-Pb isotopic system induced by fluid and/or heating can result in obtaining geologically meaningless U-Pb and Th-Pb dates, which may lead to significant misinterpretations in
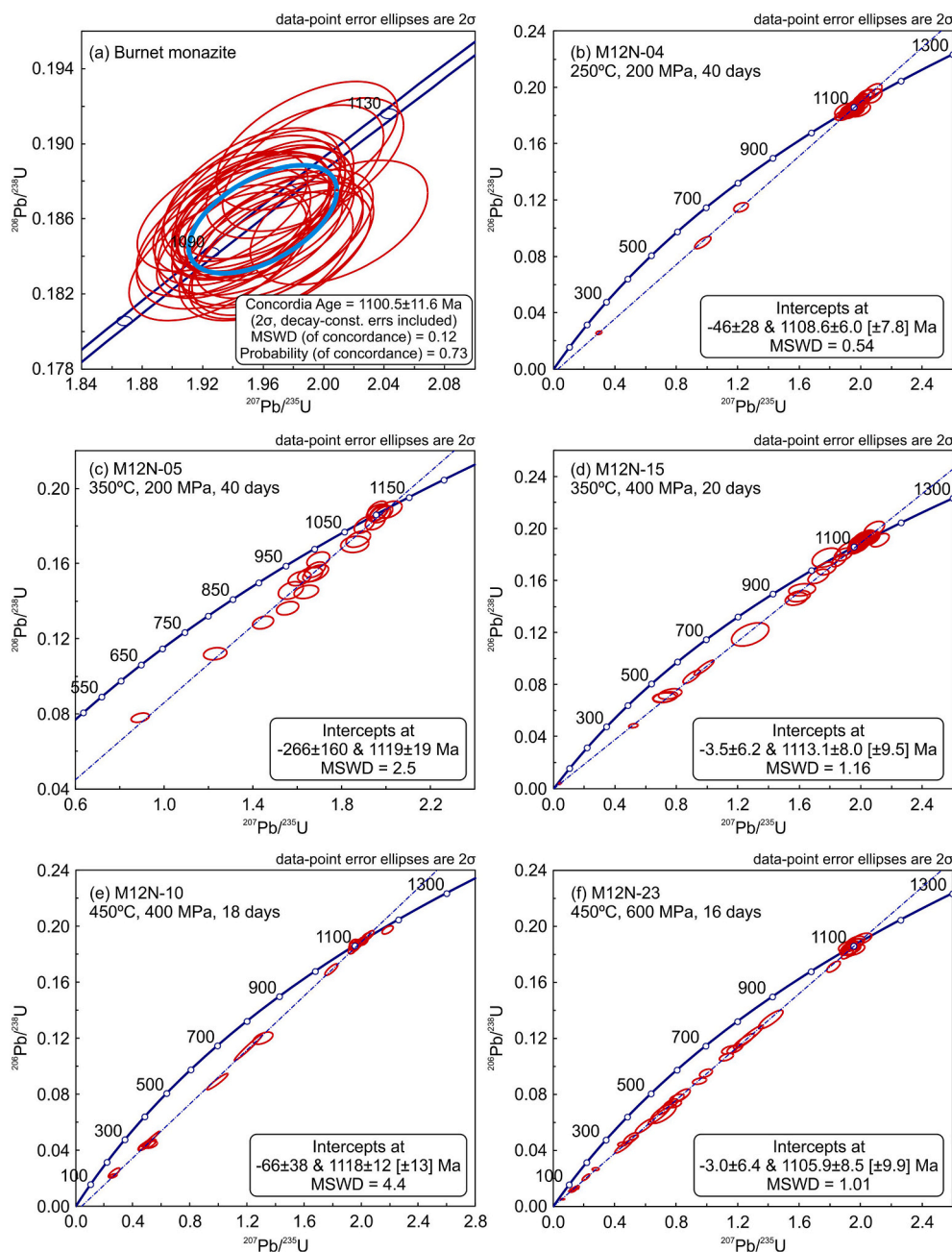
Fig. 10. Concordia plots presenting summary of LA-ICP-MS U-Pb isotopic data of (a) the Burnet monazite used as starting material and (b–l) the monazite from experimental products. See text for explanations.

petrochronological reconstructions. The presented TEM, Raman and LA-ICPMS U-Th-Pb data from experimentally altered monazite present a complementary overview and provide new insights on the fluid-mediated alteration processes affecting the U-Th-Pb age record in monazite under broad temperature conditions.

4.1. TEM and Raman evaluation of radiation damage and fluid-induced alteration

The TEM data revealed various processes that affected monazite, which were induced by either temperature or fluid, or both. The distorted crystal integrity in the Burnet monazite observed as mottled diffraction contrast in TEM images and smeared out diffraction patterns, reflects moderate degree of radiation damage (Fig. 3e), which is a common feature of natural monazite (cf., Seydoux-Guillaume et al.,

2002, 2003, 2007, 2012, 2018; Grand'Homme et al., 2016, 2018; Nasdala et al., 2020). The Burnet monazite is particularly susceptible to this process due to its high content of Th and U and old age, whereas such mottled contrast domains are usually absent in young monazite crystals (cf., Seydoux-Guillaume et al., 2004). The presented TEM data also confirmed that unaltered monazite preserves a significant degree of radiation damage at 450 and 550 °C. On the other hand, the fluid-mediated alteration at 450–550 °C resulted in recrystallization of monazite observed in TEM imaging and Raman data with very low FWHM values, indicating a high degree of structural order in the altered, patchy domains of monazite. Similar fluid-aided replacement of the primary monazite by secondary monazite has been observed in TEM-BF imaging of monazite from experiments at 500 °C (Grand'Homme et al., 2018).

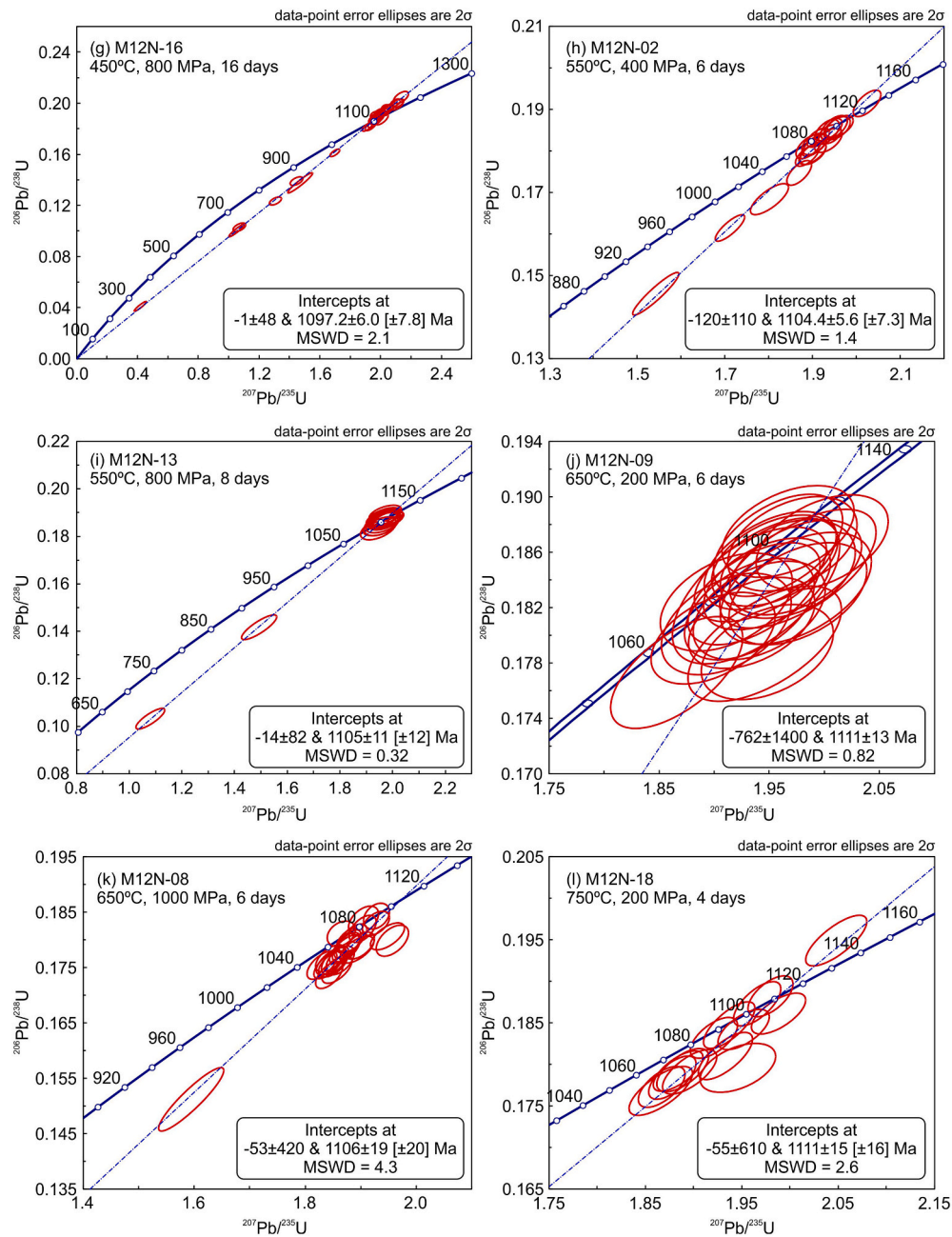The Raman data presenting decreasing FWHM values of $\nu_1(PO_4)$

Fig. 10. (*continued*).

stretching band ca. 974 cm^{-1} from 13.94–15.66 cm^{-1} to 12.81–14.39 cm^{-1}, 11.02–12.38 cm^{-1} and 7.07–7.16 cm^{-1} in the unaltered domains of monazite from runs at 450, 550, 650 and 750 °C, respectively, which are significantly lower than 18.23–20.28 cm^{-1} in the Burnet monazite, demonstrate temperature dependence of the annealing of radiation damage in monazite. Comparing these results to FWHM values of 7.46–8.76 cm^{-1} and 7.55–10.56 cm^{-1} (Burnet monazite and unaltered domains from runs at 450–750 °C, respectively) calculated using empirical equation that provides theoretical FWHM values for non-radiation damaged monazite, indicates that temperature conditions of 450–550 °C are not sufficient for a significant annealing and healing of the crystal structure. These results are generally consistent with a previous study on experimental annealing of natural monazite reporting FWHM values of ν_1(PO$_4$) stretching band from 15.0 ± 1.0 cm^{-1} in untreated monazite to 12.6 ± 1.0, 5.8 ± 0.7 and 5.7 ± 0.7 cm^{-1} for

monazite annealed at 500, 800 and 900 °C, respectively (Seydoux-Guillaume et al., 2002).

Monazite from experiments at 650 and 750 °C provided important information that fluid-mediated alteration does not result in the development of patchy domains at these conditions. Instead, a temperature-induced homogenization and annealing of the monazite structure occurred at 650 °C, indicated by the presence of weak mottled diffraction contrast and sharp diffraction patterns (Fig. 8c–e). Simultaneous alteration induced by fluid resulted in the formation of lenticular microporosity oriented along the cleavage, which eventually proceeded further to partially replace the monazite (both the rim and the core) by secondary fluorcalciobritholite and cheralite (Fig. 1k, 8). The alteration processes at 650 °C were accompanied by partial melting of the starting materials in the experimental capsule. In contrast, the monazite alteration at 750 °C accompanied by strong melting during experiment was
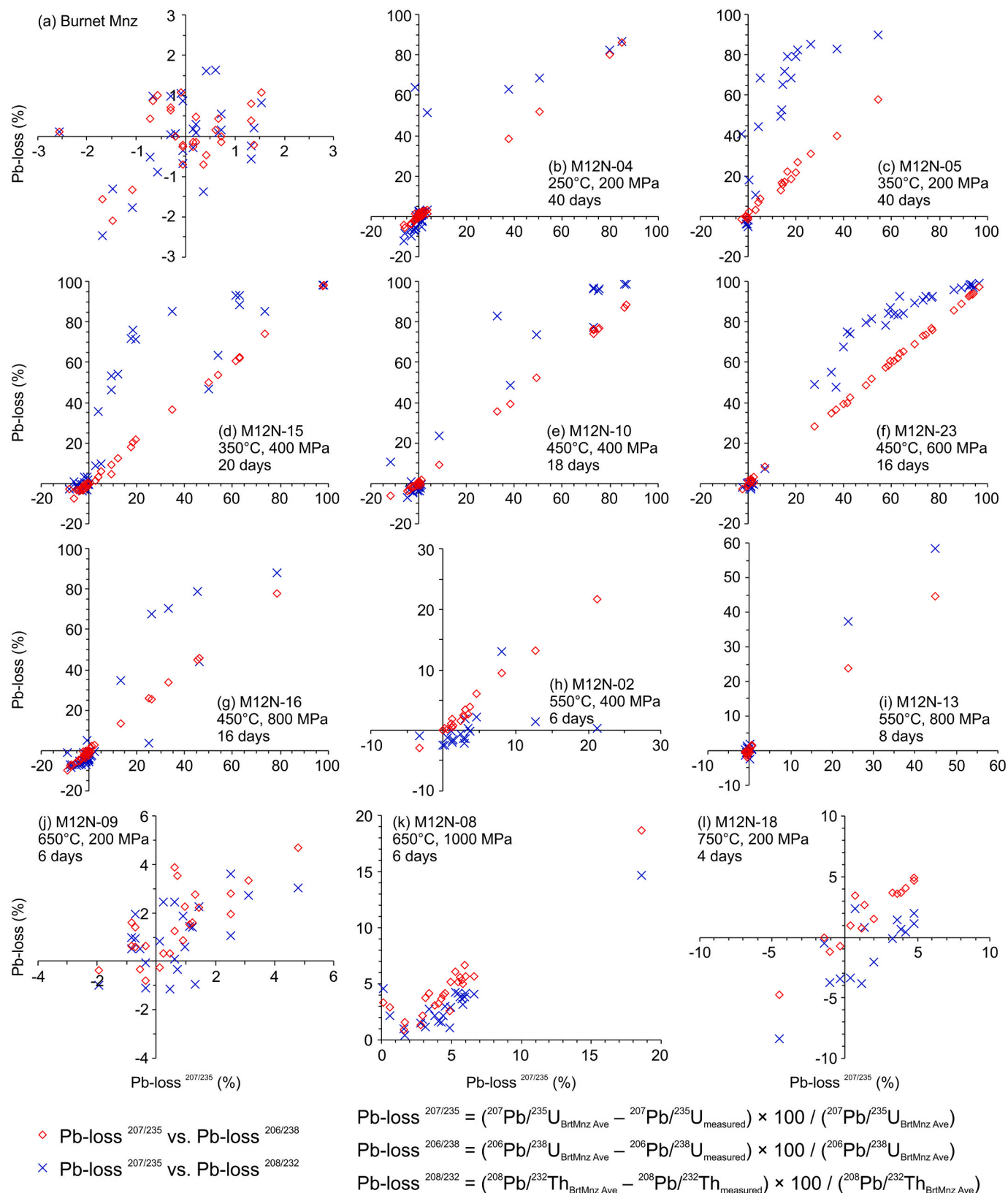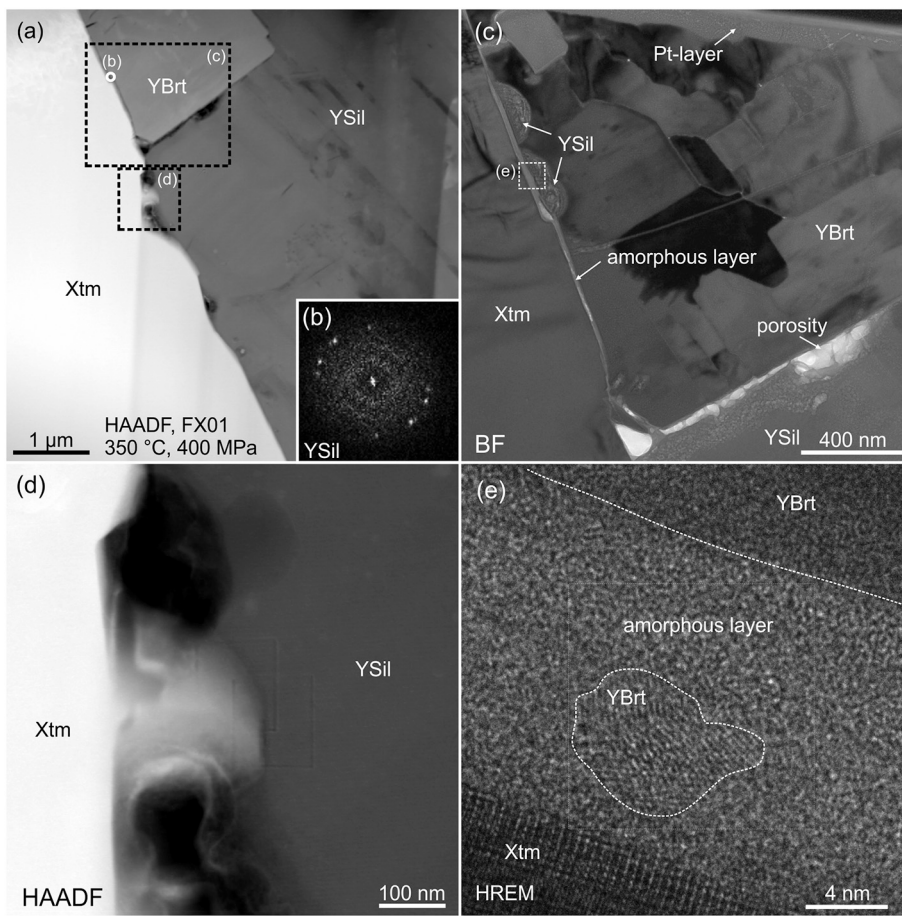
Fig. 11. Diagrams of the Pb-loss$^{207/235}$ vs. Pb-loss$^{206/238}$ and Pb-loss$^{208/232}$. In general, the Pb-loss$^{207/235}$ data correlate linearly with the Pb-loss$^{206/238}$, and exponentially with Pb-loss$^{208/232}$, which indicates significant fractionation between Pb/U and Pb/Th isotopic systems.

Fig. 12. TEM images of xenotime (FIB-foil FX01, 350 °C and 400 MPa). (a) HAADF image of the phase boundary between xenotime (Xtm), Y-rich fluorcalciobritholite (YBrt) and unidentified (Y, HREE)-rich silicate (YSil). (c) BF image presenting an amorphous layer between xenotime and polycrystalline Y-rich fluorcalciobritholite. (d) The interface between xenotime and unidentified Y-rich silicate with partial dissolution of the xenotime surface. (e) HREM image of the amorphous layer between xenotime and Y-rich fluorcalciobritholite with the nucleating nanocrystal of Y-rich fluorcalciobritholite.

significantly different and more intense. The presence of flame-like microtextures demonstrates a migrating alteration front due to the coupled dissolution-reprecipitation reaction, which resulted in the replacement of monazite by fluorcalciobritholite, REE-rich fluorapatite and cheralite (Fig. 9). The cheralite nanocrystals on the monazite surface represent seeds for nucleation of irregular cheralite grains, which grew during progressing alteration and moving reaction front inwards monazite. Developed strong nanoporosity and nanocrystals of cheralite present in the monazite core demonstrate a significant influence of the alteration processes resulting in recrystallization of the entire monazite grain induced by temperature and fluid and/or melt. The cheralite nanocrystals present in nanopores across the monazite grain indicate that Th was transported only at a very short distance. These features, characteristic for fluid-aided coupled dissolution-reprecipitation reactions (cf., Putnis, 2002, 2009), suggest that remobilization of Th, U and Pb occurred at a short distance. Because such subtle results of the mobilization of these elements and accumulation in secondary nanocrystals cannot be noticed using standard EPMA-BSE imaging due to insufficient resolution, they may strongly affect interpretations of the geochronological results.

TEM and Raman study of xenotime demonstrated significant differences compared to the results for monazite. TEM investigations have shown that alteration and partial replacement by either unidentified (Y, HREE)-rich silicate at 350 °C or by Y-rich fluorcalciobritholite at 650 °C affected the xenotime grains along and within limited extend near the surface or along the cracks (Fig. 2). No transformations occurred within the xenotime crystalline structure (Figs. 12, 13), compared to those observed in the monazite. Another aspect of the TEM and Raman data is the absence of any features of radiation damage. The NWFP xenotime and xenotime from experiments have a crystal structure without

significant defects visible in TEM imaging. Raman data, i.e. FWHM values of Raman $\nu_1(PO_4)$ stretching band ca. 1000 cm^{-1}, also show no broadening which may suggest even low degree of radiation damage. Our TEM and Raman results confirm observations from earlier experiments involving NWFP xenotime, that is well crystalline and not affected by metamictization (Harlov and Wirth, 2012). Lack of radiation damage is related to low contents of U and Th, which is a common feature in xenotime. As a consequence, the disturbance of the U-Th-Pb system is very rare compared to monazite (cf., Kositcin et al., 2003; Rasmussen et al., 2004, 2011; Švecová et al., 2016; Budzyń et al., 2018). Nevertheless, xenotime in general is a robust geochronometer due to lack of crystalline defects enhanced by radiation damage, in opposite to monazite, which is a much better target for alkali-bearing fluids that relatively easily induce compositional alteration and age disturbance.

4.2. Implications for monazite geochronology

The results of isotopic LA-ICPMS U-Th-Pb measurements provide new insights into monazite geochronology. Because monazite forms under a wide range of P-T conditions, in-situ U-Th-Pb analysis combined with the textural setting of individual grains or internal domains allows constraining the age of particular igneous and metamorphic processes or deformations (Williams et al., 2007, 2017). Despite of the high closure temperature of Pb diffusion, the isotopic U-Th-Pb system in monazite may be disturbed under conditions corresponding to middle- to upper crustal depths due to metasomatic alteration (Cherniak et al., 2004). In addition, recent studies have shown that monazite can accumulate substantial amounts of common or initial Pb (Seydoux-Guillaume et al., 2012; Skrzypek et al., 2017; Jastrzębski et al., 2021; Barnes et al., 2021; Budzyń et al., 2021). Previous experimental studies demonstrated that
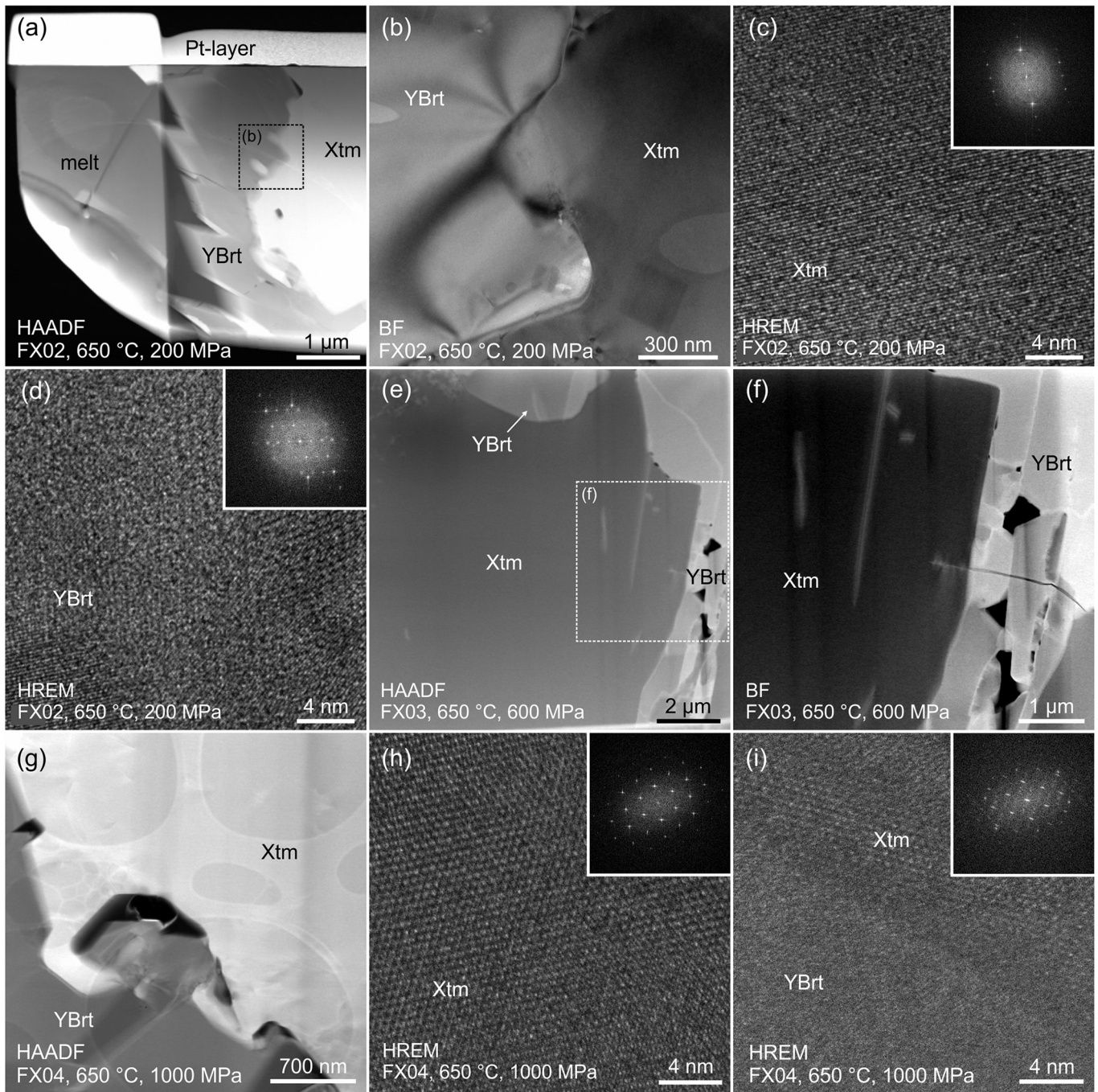
Fig. 13. TEM images of xenotime from three experiments at 650 °C (FIB-foils FX02, 650 °C and 200 MPa; FX03, 650 °C and 600 MPa; FX04, 650 °C, 1000 MPa). (a) HAADF, (b) BF and (c, d) HREM images showing the interface between crystalline xenotime and Y-rich fluorcalciobritholite; Y-rich fluorcalciobritholite has a distorted structure represented by a mottled diffraction pattern and diffuse diffraction centers. (e) HAADF and (f) BF images of xenotime overgrown with Y-rich fluorcalciobritholite. (g) HAADF and (h, i) HREM lattice fringe images of the xenotime-britholite interface, displaying the change in crystallinity at the phase boundary.

alteration induced by alkali-rich fluids via coupled dissolution-reprecipitation reactions result in incomplete removal of Pb in the temperature range from 250 °C to 600 °C (Budzyń et al., 2015, 2017; Grand'Homme et al., 2016) or nearly complete removal of Pb at 450 °C (Williams et al., 2011). Investigation of the natural processes requires understanding the mechanisms and the effects of alteration due to mineral-fluid reactions. The LA-ICPMS or SIMS U-Th-Pb analysis applied to the monazite population with a broad range of discordant ages and various degree of Pb-loss is a powerful tool to constrain the age of

metasomatic processes. The LA-ICPMS data from this study have shown that coupled dissolution-reprecipitation reactions that induced removal of Pb were enhanced mostly by temperature resulting in various degree of U-Th-Pb disturbance in monazite (from weak at 250 °C, to moderate or strong at 350, 450 and 550 °C) and only a few analyses indicate nearly complete Pb-loss. The variable degree of Pb-loss is related to the duration of experiments, which is way shorter than that of geological processes in nature, and to the presence of submicron remains of the unaltered monazite within the altered domains (cf., Grand'Homme

et al., 2018). The main factors controlling Pb-loss in monazite include intensity of radiation damage, temperature conditions, composition of fluid and bulk composition of rock (or here – the capsule charge). Such combination of complex factors have to be carefully investigated to avoid misinterpretations of monazite geochronology in natural samples.

The altered monazite domains revealed also significant differences within individual isotopic dates, i.e. the $^{208}Pb/^{232}Th$ isotopic ratios indicate apparent higher loss of Pb than those related to $^{207}Pb/^{235}U$ and $^{206}Pb/^{238}U$ ratios. The discrepancy between Th-Pb and U-Pb data demonstrate high isotopic fractionation and higher mobility of ^{208}Pb than that of ^{207}Pb and ^{206}Pb during experimental alteration of monazite (Fig. 11b–i), showing that both isotopic systems should be considered carefully in monazite geochronology. The importance of the conducted LA-ICPMS U-Pb measurements is that the results reveal general trends of linear regression with the lower intercepts on the Concordia plots of approximately 0 Ma, which is the age of the experiment. These confirm a high potential of in-situ U-Th-Pb measurements within monazite population to constrain the age of the metasomatic processes. The precision of the lower intercept age increases over time in natural samples compared to those observed in this work. This is due to progressive accumulation of radiogenic Pb in geological samples after the U-Th-Pb clock is reset during alteration (cf., the precision of lower intercept age of altered xenotime of 368 ± 6 Ma; Budzyń et al., 2018).

The investigated monazite from experiments under temperature conditions at 650 °C and 750 °C has particular importance with respect to the preservation of age record during high-grade processes. Partial to complete resetting of the monazite age is generally related to processes at low- to moderate temperature conditions (250–600 °C; Williams et al., 2011; Budzyń et al., 2015; Grand'Homme et al., 2016, 2018), whereas monazite is considered to be rather resistant to disturbance of U-Th-Pb isotopic system in granitic and metamorphic rocks under conditions above ca. 600 °C up to the closure temperature. Here, the investigated monazite from experiments at 650 °C and 750 °C demonstrated weak to strong alteration during TEM investigations, despite no compositional or textural features indicating alteration during EPMA evaluation. The submicron scale observations correspond to an initial disturbance of the U-Pb isotopic record (Fig. 10j–l) and partial Pb-loss of ca. 5–7% (with even one analysis of 18.6%) or Pb-gain of up to 8.4% (Fig. 11j–l, Table 3). Furthermore, our TEM and Raman data support the conclusion that Pb-loss and age rejuvenation were enhanced by combination of annealing and coupled dissolution-reprecipitation processes, and should not be misinterpreted as related to diffusion. The results of TEM and LA-ICPMS study of the experimentally altered monazite over 4–6 days provide important implications for monazite geochronology of high-grade metamorphic processes. Several days duration of the experiment cannot be compared to duration of natural processes in geological time, which implies that recrystallization of monazite may result in more or less pronounced discordance of U-Th-Pb isotopic system and partial to complete resetting of the age record. A recent petrochronological study revealed an isotopic disturbance in monazite from granulite during high-grade metamorphism overprint (Jastrzębski et al., 2021). Despite the lack of textural evidence of monazite alteration in BSE imaging, the isotopic LA-ICPMS U-Th-Pb analysis revealed relatively high disturbance of the age record and addition of common Pb interpreted as partially induced by high temperature conditions of ca. 850 °C (Jastrzębski et al., 2021). All these facts suggest that the interpretation of monazite ages in high grade rocks, particularly those affected by multiple thermal events, should be taken with great caution. Potential fluid- or melt-induced processes can occur at the nanometer-scale and result in isotopic alteration that may not be recognized as the result of alteration in BSE imaging and compositional X-ray mapping.

5. Conclusions

The presented data provide important insights into the monazite

geochronology of metamorphic, magmatic and post-magmatic processes. Raman data demonstrate that the degree of annealing of radiation damage in the monazite structure increases with increasing temperature, which is consistent with earlier studies. Metasomatic alteration at 250–550 °C resulted in low to high discordance of the U-Th-Pb isotopic system and various degrees of Pb-loss (up to 99.4%) in altered monazite domains. The unaltered domains preserved the age record, whereas lower intercept U-Pb ages of the altered domains population provide the age of the metasomatic alteration. Monazite from runs at 650 and 750 °C yielded U-Th-Pb data indicating initial disturbance and from 8.4% Pb-gain to 18.6% Pb-loss. Linear regressions with lower intercepts of −53 ± 420 Ma and −55 ± 610 Ma roughly correspond to the timing of the experiments. This demonstrates that application of the U-Pb isotopic analysis on the population of altered monazite with disturbed ages can be used to constrain the age of metasomatic event. It also highlights the potential of utilizing the discordant data, that are often discarded in geochronology papers to publish only "nice" and concordant data, thus often losing very important information about later geological processes. Additional care should be given to a comparison of U-Pb and Th-Pb dates due to fractionation of the corresponding isotopes during alteration. The particular outcome of this study is that processes at 650–750 °C involve combination of annealing of the radiation damaged structure and an alkali-bearing fluid-induced compositional alteration within entire monazite grains at the submicron level. These may remain unnoticed when using standard microanalytical techniques, however, these processes can result in disturbance of U-Th-Pb system causing significant misinterpretations in reconstruction of geological processes. To summarize, it is important to understand monazite mineralogy in order to use monazite dating in tectonic reconstructions, which is a direct link from submicron-scale to km-scale geochronological reconstructions.

Declaration of Competing Interest

The authors declare that they have no known competing financial interests or personal relationships that could have appeared to influence the work reported in this paper.

Appendix A. Supplementary data

Supplementary data to this article can be found online at https://doi.org/10.1016/j.chemgeo.2021.120464.

References

Barnes, C.J., Majka, J., Jeanneret, P., Ziemniak, G., Kooijman, E., Kośmińska, K., Kielman-Schmitt, M., Schneider, D.A., 2021. Using Th-U-Pb geochronology to extract crystallization ages of Paleozoic metamorphic monazite contaminated by initial Pb. Chem. Geol. https://doi.org/10.1016/j.chemgeo.2021.120450.

Broska, I., Siman, P., 1998. The breakdown of monazite in the West-Carpathian Veporic orthogneisses and Tatric granites. Geol. Carpath. 49, 161–167.

Broska, I., Williams, C.T., Janák, M., Nagy, G., 2005. Alteration and breakdown of xenotime-(Y) and monazite-(Ce) in granitic rocks of the Western Carpathians, Slovakia. Lithos 82, 71–83.

Budzyń, B., Kozub-Budzyń, G.A., 2015. The stability of xenotime in high Ca and Ca-Na systems, under experimental conditions of 250–350°C and 200–400 MPa: the implications for fluid-mediated low-temperature processes in granitic rocks. Geol. Q. 59, 316–324.

Budzyń, B., Sláma, J., 2019. Partial resetting of U–Pb ages during experimental fluid-induced re-equilibration of xenotime. Lithos 346–347, 105163.

Budzyń, B., Hetherington, C.J., Williams, M.L., Jercinovic, M.J., Michalik, M., 2010. Fluid-mineral interactions and constraints on monazite alteration during metamorphism. Mineral. Mag. 74, 659–681.

Budzyń, B., Harlov, D.E., Williams, M.L., Jercinovic, M.J., 2011. Experimental determination of stability relations between monazite, fluorapatite, allanite, and REE-epidote as a function of pressure, temperature, and fluid composition. Am. Mineral. 96, 1547–1567.

Budzyń, B., Kozub-Budzyń, G., 2015. Stability of monazite and disturbance of the Th-U-Pb system under experimental conditions of 250–350 °C and 200–400 MPa. Ann. Soc. Geol. Pol. 85, 405–424.

Budzyń, B., Harlov, D.E., Kozub-Budzyń, G., Majka, J., 2017. Experimental constraints on the relative stabilities of the two systems monazite-(Ce) – allanite-(Ce) – fluorapatite and xenotime-(Y) – (Y,HREE)-rich epidote – (Y,HREE)-rich fluorapatite, in high Ca and Na-Ca environments under P-T conditions of 200–1000. Mineral. Petrol. 111, 183–217.

Budzyń, B., Sláma, J., Kozub-Budzyń, G.A., Konečný, P., Holický, I., Rzepa, G., Jastrzębski, M., 2018. Constraints on the timing of multiple thermal events and re-equilibration recorded by high-U zircon and xenotime: case study of pegmatite from Piława Górna (Góry Sowie Block, SW Poland). Lithos 310–311, 65–85.

Budzyń, B., Sláma, J., Corfu, F., Crowley, J., Schmitz, M., Williams, M.L., Jercinovic, M. J., Kozub-Budzyń, G.A., Konečný, P., Rzepa, G., Włodek, A., 2021. TS-Mnz – a new monazite age reference material for U-Th-Pb microanalysis. Chem. Geol. 572, 120195.

Cherniak, K., Watson, E., Grove, M., Harrison, M.T., 2004. Pb diffusion in monazite: a progress report on a combined RBS/SIMS study. Geochim. Cosmochim. Acta 68, 829–840.

Didier, A., Bosse, V., Boulvais, P., Bouloton, J., Paquette, J.-L., Montel, J.-M., Devidal, J.-L., 2013. Disturbance versus preservation of U–Th–Pb ages in monazite during fluid–rock interaction: textural, chemical and isotopic in situ study in microgranites (Velay Dome, France). Contrib. Mineral. Petrol. 165, 1051–1072.

Finger, F., Broska, I., Roberts, M.P., Schermaier, A., 1998. Replacement of primary monazite by apatite-allanite-epidote coronas in an amphibolite facies granite gneiss from the eastern Alps. Am. Mineral. 83, 248–258.

Finger, F., Krenn, E., Schulz, B., Harlov, D., Schiller, D., 2016. "Satellite monazites" in polymetamorphic basement rocks of the Alps: their origin and petrological significance. Am. Mineral. 101, 1094–1103.

Grand'Homme, A., Janots, E., Seydoux-Guillaume, A.-M., Guillaume, D., Bosse, V., Magnin, V., 2016. Partial resetting of the U-Th-Pb systems in experimentally altered monazite: nanoscale evidence of incomplete replacement. Geology 44, 431–434.

Grand'Homme, A., Janots, E., Seydoux-Guillaume, A.M., Guillaume, D., Magnin, V., Hövelmann, J., Höschen, C., Boiron, M.C., 2018. Mass transport and fractionation during monazite alteration by anisotropic replacement. Chem. Geol. 484, 51–68.

Harlov, D.E., Hetherington, C.J., 2010. Partial high-grade alteration of monazite using alkali-bearing fluids: experiment and nature. Am. Mineral. 95, 1105–1108.

Harlov, D.E., Wirth, R., 2012. Experimental incorporation of Th into xenotime at middle to lower crustal P-T utilizing alkali-bearing fluids. Am. Mineral. 97, 641–652.

Harlov, D.E., Wirth, R., Hetherington, C.J., 2011. Fluid-mediated partial alteration in monazite: the role of coupled dissolution-reprecipitation in element redistribution and mass transfer. Contrib. Mineral. Petrol. 162, 329–348.

Hetherington, C.J., Harlov, D.E., 2008. Metasomatic thorite and uraninite inclusions in xenotime and monazite from granitic pegmatites, Hidra anorthosite massif, southwestern Norway: mechanics and fluid chemistry. Am. Mineral. 93, 806–820.

Hetherington, C.J., Jercinovic, M.J., Williams, M.L., Mahan, K., 2008. Understanding geologic processes with xenotime: composition, chronology, and a protocol for electron microprobe microanalysis. Chem. Geol. 254, 133–147.

Hetherington, C.J., Harlov, D.E., Budzyń, B., 2010. Experimental metasomatism of monazite and xenotime: mineral stability, REE mobility and fluid composition. Mineral. Petrol. 99, 165–184.

Holder, R.M., Hacker, B.R., Kylander-Clark, A.R.C., Cottle, J.M., 2015. Monazite trace-element and isotopic signatures of (ultra)high-pressure metamorphism: examples from the Western Gneiss Region, Norway. Chem. Geol. 409, 99–111.

Horstwood, M.S.A., Košler, J., Gehrels, G., Jackson, S.E., McLean, N.M., Paton, Ch., Pearson, N.J., Sircombe, K., Sylvester, P., Vermeesch, P., Bowring, J.F., Condon, D.J., Schoene, B., 2016. Community-derived standards for LA-ICP-MS U-(Th-)Pb geochronology – uncertainty propagation, age interpretation and data reporting. Geostand. Geoanal. Res. 40, 311–332.

Janots, E., Engi, M., Berger, A., Allaz, J., Schwarz, J.O., Spandler, C., 2008. Prograde metamorphic sequence of REE minerals in pelitic rocks of the Central Alps: implications for allanite–monazite–xenotime phase relations from 250 to 610°C. J. Metamorph. Geol. 26, 509–526.

Jastrzębski, J., Żelaźniewicz, A., Budzyń, B., Sláma, J., Konečny, P., 2020. Age constraints on the Pre-Variscan and Variscan thermal events in the Kamieniec

Ząbkowicki Metamorphic belt (the Fore-Sudetic Block, SW Poland). Ann. Soc. Geol. Pol. 90, 27–49.

Jastrzębski, M., Budzyń, B., Żelaźniewicz, A., Konečný, P., Sláma, J., Kozub-Budzyń, G. A., Skrzypek, E., Jaźwa, A., 2021. Eo-Variscan metamorphism in the Bohemian Massif: thermodynamic modeling and monazite geochronology of gneisses and granulites of the Góry Sowie Massif, SW Poland. J. Metamorphic Geol. 39, 751–779. https://doi.org/10.1111/JMG.12589.

Kositcin, N., McNaughton, N.J., Griffin, B.J., Fletcher, I.R., Groves, D.I., Rasmussen, B., 2003. Textural and geochemical discrimination between xenotime of different origin in the Archaean Witwatersrand Basin, South Africa. Geochim. Cosmochim. Acta 67, 709–731.

Kylander-Clark, A.R.C., 2017. Petrochronology by laser-ablation inductively coupled plasma mass spectrometry. In: Kohn, M.J., Engi, M., Lanari, P. (Eds.), Petrochronology: Methods and Applications. Reviews in Mineralogy and Geochemistry, 83, pp. 183–198.

Li, X.-Ch., Yang, K.-F., Spandler, C., Fan, H.-R., Zhou, M.-F., Hao, J.-L., Yang, Y.-H., 2021. The effect of fluid-aided modification on the Sm-Nd and Th-Pb geochronology of monazite and bastnäsite: implication for resolving complex isotopic age data in REE ore systems. Geochim. Cosmochim. Acta 300, 1–24.

Ludwig, K.R., 2012. Isoplot 3.75. A Geochronological Toolkit for Microsoft Excel, 5. Berkeley Geochronological Center, Special Publication, pp. 1–75.

Nasdala, L., Wenzel, M., Vavra, G., Irmer, G., Wenzel, T., Kober, B., 2001. Metamictisation of natural zircon: accumulation versus thermal annealing of radioactivity-induced damage. Contrib. Mineral. Petrol. 141, 125–144.

Nasdala, L., Akhmadaliev, S., Burakov, B.E., Chanmuang, N., Škoda, R., 2020. The absence of metamictisation in natural monazite. Sci. Rep. 10, 14676.

Parrish, R.R., 1990. U-Pb dating of monazite and its application to geological problems. Can. J. Earth Sci. 27 (11), 1431–1450.

Putnis, A., 2002. Mineral replacement reactions: from macroscopic observations to microscopic mechanisms. Mineral. Mag. 66, 689–708.

Putnis, A., 2009. Mineral replacement reactions. In: Oelkers, E.H., Schott, J. (Eds.), Thermodynamics and Kinetics of Water-Rock Interaction. Reviews in Mineralogy and Geochemistry, 70 (1), pp. 87–124.

Rasmussen, B., 2005. Radiometric dating of sedimentary rocks: the application of diagenetic xenotime geochronology. Earth Sci. Rev. 68, 197–243.

Rasmussen, B., Fletcher, I.R., Bengston, S., McNaughton, N.J., 2004. SHRIMP U–Pb dating of diagenetic xenotime in the Stirling Range Formation, Western Australia: 1.8 billion year minimum age for the Stirling biota. Precambrian Res. 133, 329–337.

Rasmussen, B., Fletcher, I.R., Muhling, J.R., 2011. Response of xenotime to prograde metamorphism. Contrib. Mineral. Petrol. 162, 1259–1277.

Ruschel, K., Nasdala, L., Kronz, A., Hanchar, J.M., Többens, D.M., Škoda, R., Finger, F., Möller, A., Ruschel, K., Nasdala, L., Kronz, A., Hanchar, J.M., Többens, D.M., Škoda, R., Finger, F., Möller, A., 2012. A Raman spectroscopic study on the structural disorder of monazite-(Ce). Mineral. Petrol. 105, 41–55.

Schaltegger, U., Wotzlaw, J.-F., Ovtcharova, M., Chiaradia, M., Spikings, R., 2014. Mass spectrometry in earth sciences: the precise and accurate measurement of time. Chimia 68, 124–128.

Schmitt, A.K., Vazquez, J.A., 2017. Secondary ion mass spectrometry analysis in petrochronology. In: Kohn, M.J., Engi, M., Lanari, P. (Eds.), Petrochronology: Methods and Applications. Reviews in Mineralogy and Geochemistry, 83, pp. 199–230.

Schoene, B., 2014. U–Th–Pb geochronology. In: Holland, H.D., Turekian, K.K. (Eds.), Treatise on Geochemistry, Elsevier, Second edition, 4.10, pp. 341–378.

Seydoux-Guillaume, A.M., Wirth, R., Heinrich, W., Montel, J.-M., 2002. Experimental determination of Thorium partitioning between monazite and xenotime using analytical electron microscopy and X-ray diffraction Rietveld analysis. Eur. J. Mineral. 14, 869–878.

Seydoux-Guillaume, A.M., Goncalves, P., Wirth, R., Deutsch, A., 2003. Transmission electron microscope study of polyphase and discordant monazites: site-specific specimen preparation using the focused ion beam technique. Geology 31, 973–976.

Seydoux-Guillaume, A.M., Wirth, R., Deutsch, A., Schärer, U., 2004. Microstructure of 24–1928 Ma concordant monazites; implications for geochronology and nuclear waste deposits. Geochim. Cosmochim. Acta 68, 2517–2527.

Seydoux-Guillaume, A.-M., Wirth, R., Ingrin, J., 2007. Contrasting response of ThSiO$_4$ and monazite to natural irradiation. Eur. J. Mineral. 19, 7–14.

Seydoux-Guillaume, A.-M., Montel, J.-M., Bingen, B., Bosse, V., De Parseval, P., Paquette, J., Janots, E., Wirth, R., 2012. Low-temperature alteration of monazite: fluid mediated coupled dissolution–precipitation, irradiation damage, and disturbance of the U–Pb and Th–Pb chronometers. Chem. Geol. 330–331, 140–158.

Seydoux-Guillaume, A.-M., Deschanels, X., Baumier, C., Neumeier, S., Weber, W.J., Peuget, S., 2018. Why natural monazite never becomes amorphous: experimental evidence for alpha self-healing. Am. Mineral. 103, 824–827.

Skrzypek, E., Bosse, V., Tetsuo Kawakami, T., Martelat, J.E., Štípská, P., 2017. Transient allanite replacement and prograde to retrograde monazite (re)crystallization in medium-grade metasedimentary rocks from the Orlica-Śnieżnik Dome (Czech Republic/Poland): textural and geochronological arguments. Chem. Geol. 449, 41–57.

Švecová, E., Čopjaková, R., Losos, Z., Škoda, R., Nasdala, L., Cícha, J., 2016. Multi-stage evolution of xenotime–(Y) from Písek pegmatites, Czech Republic: an electron probe micro-analysis and Raman spectroscopy study. Mineral. Petrol. 110, 747–765.

Villa, I.M., Williams, M.L., 2013. Geochronology of metasomatic events. In: Harlov, D.E., Austrheim, H. (Eds.), Metasomatism and the Chemical Transformation of Rock. Springer, Heidelberg, pp. 171–202. https://doi.org/10.1007/978-3-642-28394-9.

Williams, M.L., Jercinovic, M.J., Hetherington, C.L., 2007. Microprobe monazite geochronology: understanding geologic processes by integrating composition and chronology. Annu. Rev. Earth Planet. Sci. 35, 137–175.

Williams, M.L., Jercinovic, M.J., Harlov, D.E., Budzyń, B., Hetherington, C.J., 2011. Resetting monazite ages during fluid-related alteration. Chem. Geol. 283, 218–225.

Williams, M.L., Jercinovic, M.J., Mahan, K.H., Dumond, G., 2017. Electron microprobe petrochronology. In: Kohn, M.J., Engi, M., Lanari, P. (Eds.), Petrochronology: Methods and Applications. Reviews in Mineralogy and Geochemistry, 83, pp. 153–182.

Wirth, R., 2004. Focused Ion Beam (FIB): a novel technology for advanced application of micro- and nanoanalysis in geosciences and applied mineralogy. Eur. J. Mineral. 16, 863–876.

Wirth, R., 2009. Focused Ion Beam (FIB) combined with SEM and TEM: Advanced analytical tools for studies of chemical composition, microstructure and crystal structure in geomaterials on a nanometre scale. Chem. Geol. 261, 217–229.